



Review

Recent Applications of Advanced Atomic Force Microscopy in Polymer Science: A Review

Phuong Nguyen-Tri ^{1,2,*}, Payman Ghassemi ², Pascal Carriere ³, Sonil Nanda ⁴ ,
Aymen Amine Assadi ⁵ and Dinh Duc Nguyen ^{6,7} 

¹ Institute of Research and Development, Duy Tan University, Da Nang 550000, Vietnam

² Département de Chimie, Biochimie et Physique, Université du Québec à Trois-Rivières (UQTR),
Trois-Rivières, QC G8Z 4M3, Canada; payman.ghassemi3@gmail.com

³ Laboratoire MAPIEM (EA 4323), Matériaux Polymères Interfaces Environnement Marin, Université de
Toulon, CEDEX 9, 83041 Toulon, France; pascal.carriere@univ-tln.fr

⁴ Department of Chemical and Biological Engineering, University of Saskatchewan, Saskatoon, SK S7N 5A2,
Canada; sonil.nanda@usask.ca

⁵ ENSCR—Institut des Sciences Chimiques de Rennes (ISCR)—UMR CNRS 6226, Univ Rennes, 35700 Rennes,
France; aymen.assadi@ensc-rennes.fr

⁶ Faculty of Environmental and Food Engineering, Nguyen Tat Thanh University, 300A Nguyen Tat Thanh,
District 4, Ho Chi Minh City 755414, Vietnam; nguyensyduc@gmail.com

⁷ Department of Environmental Energy Engineering, Kyonggi University, Suwon 16227, Korea

* Correspondence: Phuong.nguyen-tri@uqtr.ca; Tel.: +819-376-5011 (ext. 4505)

Received: 5 March 2020; Accepted: 13 May 2020; Published: 17 May 2020



Abstract: Atomic force microscopy (AFM) has been extensively used for the nanoscale characterization of polymeric materials. The coupling of AFM with infrared spectroscopy (AFM-IR) provides another advantage to the chemical analyses and thus helps to shed light upon the study of polymers. This paper reviews some recent progress in the application of AFM and AFM-IR in polymer science. We describe the principle of AFM-IR and the recent improvements to enhance its resolution. We also discuss the latest progress in the use of AFM-IR as a super-resolution correlated scanned-probe infrared spectroscopy for the chemical characterization of polymer materials dealing with polymer composites, polymer blends, multilayers, and biopolymers. To highlight the advantages of AFM-IR, we report several results in studying the crystallization of both miscible and immiscible blends as well as polymer aging. Finally, we demonstrate how this novel technique can be used to determine phase separation, spherulitic structure, and crystallization mechanisms at nanoscales, which has never been achieved before. The review also discusses future trends in the use of AFM-IR in polymer materials, especially in polymer thin film investigation.

Keywords: AFM-IR; polymers; polymer composites; blends; polymer aging; nanoscale characterization; nanoscale characterization

1. Introduction

Fourier-transform infrared spectroscopy (FT-IR) is a popular spectroscopic technique used for the characterization and identification of numerous materials, especially for the polymers, biomaterials and life sciences [1–5]. However, the main drawback of the FT-IR method relates to its low resolution (under 20 μm). Optical microscopy is also a powerful method to study the polymer morphology, but remains limited by the diffraction limit, which is proportional to the wavelength (λ) of light:

$$\Delta x \gg 0.61 \cdot \frac{\lambda}{n \cdot \sin \theta} \quad (1)$$

where (Δx) is the distance between the two samples and (n) represents the refractive index. Moreover, θ denotes the objective's approval angle. The value of " $n \cdot \sin\theta$ " is generally referred to as the objective's numerical aperture. Equation is obtained from Rayleigh's criterion according to which two points can be determined provided the center of one Airy disk correlates with the minimum value of the next Airy pattern [6–8]. According to Equation, the lateral resolution of IR-based microscopes is often smaller than that of visible light-based microscopes because of the longer wavelength of the mid-IR light ($\lambda = 2.5\text{--}10 \mu\text{m}$) [9].

The addition of several special devices like attenuated total reflection crystals in an infrared (IR) spectroscopy (ATR-FTIR) allows the analysis of penetration depth into the sample between 0.5 and 2 μm [10]. Nevertheless, ATR-FTIR can be only performed on a spatial resolution approaching the wavelength with a sample thickness of 3–10 μm [10–15]. In contrast, the atomic force microscope (AFM) [16] is considered a useful tool for nanoscale measurement in polymer science and engineering [17–19], especially for studying complex materials [20–29]. Various newer discoveries have been reported in the literature with this nanoscale imaging technique [30–38] for structures and polymer crystallization. However, the chemical characterization of materials is limited mostly to AFM. While AFM provides information on a material's morphology, friction behavior and adhesion at the nanoscale, it cannot provide the information on chemical composition or distribution of the functional groups of the polymer materials.

The idea of chemical modification of the probes was brought in to make them sensitive to particular molecular interactions to overcome this inherent limitation of the AFM [39]. Chemical Force Microscopy (CFM) was used for the separation between hydrophilic and hydrophobic regions [40] and interactions between particular functional groups, including such polar molecules, and acid-base interactions with resolution nanometer scales [41]. CFM uses a functionalized AFM tip with a high-quality probe. Low-quality tips can result in poor imaging with various artifacts [42]. Some important considerations include the material of the probe, nominal tip length, spring constant, and resonant frequency that suits the object [43]. More recently, a new nanoscale spectroscopy, so-called photo-induced force microscopy (PiFM) has been developed to study the gradient of optical forces during the light absorption of molecular vibrational resonances, which are applied to a high sensitive AFM.

Such recent attempts effectively break the diffraction limit of light and provide vibrational spectroscopy with a nanoscale spatial resolution that is a crucial tool for characterizing novel energy materials [44]. The coupling of Raman spectroscopic and an AFM is also reported, which is called nano-Raman or AFM-Raman [45–54]. Other techniques such as atomic force microscopy-infrared spectroscopy (AFM-IR) and infrared scattering-type scanning near-field optical microscopy (IR s-SNOM) [55–58] have also been developed to overcome these disadvantages. AFM-IR is capable of measuring and mapping the local chemical composition, which is usually below the diffraction limit to provide nanoscale images as the traditional AFM [55]. This method has been considered as an important development in sub-micrometer spectroscopies and chemical imaging. The use of this technique has shed light on many assumptions and has provided new mechanisms in the investigation of polymer materials [56,57].

Nowadays, AFM-IR is being applied for analyzing various systems including polymer blends [58,59], polymer composites [60–63], multilayer films [64], polymer thin films [65,66] and in life sciences [46,48,67–69] and other materials [55]. The AFM-IR can provide both a nanoscale AFM image and a high-resolution chemical spectrum on the sample within selected regions, thus helping to identify or qualitatively analyze many complex systems. Although there have been several review articles on the use of AFM and AFM-IR [55,70–72] in material science, there is a lack of literature regarding the usefulness of this technique in polymer science. Moreover, the information on the recent applications of AFM-IR in polymer crystallization is also lacking. The goal of this review article is to provide to readers the latest advancements in the use of AFM and AFM-IR techniques in structurally characterizing polymers blends, polymer composites and multilayers, especially on polymer aging as well as on crystallization studies.

2. The Principle of AFM and AFM-IR

AFM is a microscope used for the characterization of various processes at the nanoscale that involves investigations of quantitative single molecules [33]. AFM is an exceptional tool for studying the application of temporal shifts in the morphology of polymers. The advancement of devices operating at elevated temperatures has allowed observing in-situ of the polymer crystallization by following the crystal and spherulite growth as a function of time [73]. As an important tool, AFM was commonly used in the field of polymer crystallization. Generally, the effect of the AFM tip throughout the scan should be diminished to truly reflect the crystal morphology and crystallization mechanism [74]. It is a high-resolution tool usually with a resolution of sub-10 nm features [75,76].

AFM does not require sample staining or metal coating. Hence, it is straightforward to prepare the specimen. In many cases, it is also non-destructive. It makes images to be captured whereas a process such as melting or crystal growth occurs, providing lamellar or sub-lamellar resolution time-resolved data [77–80]. An opportunity for AFM is to study the crystallization of semi-crystalline polymers due to its enable to observe crystal melting, crystal growth and lamellar reorganizations and assembly, to see how spherulites grow, and how crystallization conditions (temperature, chemical composition and sample thickness) influence crystallization kinetics [80].

A pyramidal tip attached to a cantilever (typically 100–400 μm and made of silicon or silicon nitride) is an important sensor of AFM. The resolution of an image is determined by the geometry of the apex of the pyramidal tip. The sensor operated in two modes, i.e., contact mode and non-contact or dynamic mode. In the contact mode, the tip comes in direct contact with the surface of the sample, whereas in the dynamic mode, the tip oscillates to interact with the sample surface. The cantilever acts as a contact profilometer, which generates a pattern of the sample surface upon the displacement of the tip relative to the roughness on the surface. As the AFM tip maps the sample surface, the cantilever bends owing to the repulsive forces between the samples' surface and the tip. The cantilever also deflects due to the pressure applied to the tip and the sample creating a topography of the sample surface as a feedback loop.

The AFM-Raman technique has recently emerged as an advanced tool to image the specimen topography and roughness at a nanoscale through AFM as well as chemical composition and functional groups through Raman spectroscopy. Tip-enhanced Raman scattering (TERS) uses local surface plasmon resonance effects at the probe tip to acquire physicochemical information including covalent bonding via non-metric spatial resolution. TERS is found to be promising for characterizing 1D and 2D nanomaterials, semiconductors, organic compounds and polymers.

2.1. AFM Scanning/Operation Modes

AFM can be operated under various modes, while the choice of suitable operating mode depends on the desired information and types of AFM image. In summary, there are three main operation modes of AFM, such as tapping mode, contact mode and non-contact mode. In addition to their static or dynamic nature, the three modes depend on the proximity and interactions between the sample surface and the tip (Figure 1) [81].

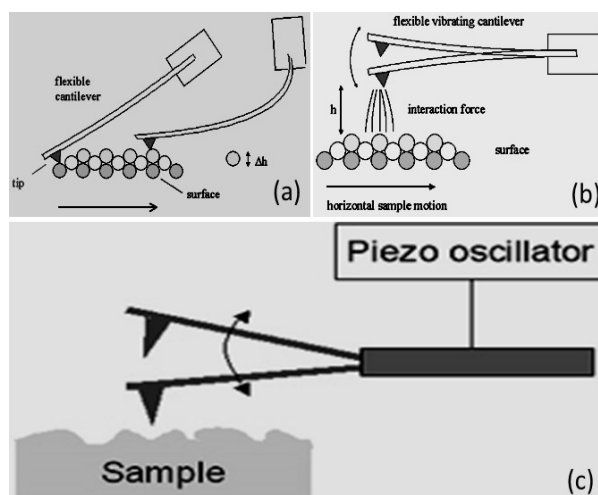


Figure 1. Different modes of scanning in an AFM: (a) contact mode; (b) non-contact mode, and (c) tapping mode. *The figure is designed by the authors.*

2.1.1. Contact Mode

Contact is mostly named a static mode, while some researchers prefer to designate the operating modes through their detection mechanisms [82]. It is characterized by a permanent repulsive interaction between the tip and the sample. The tip ‘follows’ the relief of the surface in the manner of a feeler device. The main advantages of this operation mode are the speed, the simplicity of implementation, and the possibility of simultaneously measuring another parameter, i.e., mechanical (friction) or electrical (resistance). Its notable drawbacks are the possible damage to fragile samples, the rapid wear of certain tip coatings, as well as the inconvenience linked to the presence of contamination on the surfaces [83].

2.1.2. Non-Contact Mode

In this operating mode, the cantilever vibrates at its natural resonant frequency and low amplitude away from the sample surface. Approaching it, the attractive and repulsive forces modify the resonance frequency of the lever coupled to the surface. Controlling this frequency makes it possible to regulate the tip and sample distance. It then becomes possible to map the surface of the sample.

For non-contact operation mode, a vacuum is not always required compared with scanning electron microscopy (SEM) or transmission electron microscopy (TEM) and the samples can be scanned in a liquid medium or air. These advantages have made AFM ideal for research biomaterials in the native or quasi-native environment as well as in real-time and samples can be pictured in liquid or surface air. The major advantage of this technique is that it does not cause any tip wear or damage to the sample. Its main drawback is poorer spatial resolution. It should be noted that by working with conductive or magnetic tips, it is possible to be sensitive to variations in electrostatic or magnetic forces (e.g., electrostatic force microscopy (EFM) and magnetic force microscopy (MFM)). Having experience with this mode indicated that soft materials can be easily damaged due to the shearing deformation and/or large normal force. Also, a sharp tip apex may destroy due to the imaging of a rigid sample in contact mode [84].

2.1.3. Tapping Mode

This mode was developed to improve the resolution compared to the non-contact mode. For this, the operating principle remains the same, but with greater amplitude of oscillation so that at each cycle the tip crosses the attractive area until it strikes the sample at the edge of the repellant area. At the usual frequencies of this technique (100–300 kHz), it is only in contact with the surface over very short time intervals, thus making it possible to minimize the effect of lateral forces compared to the contact mode. Soft and/or fragile samples are, therefore, not damaged, and objects weakly anchored to the surface

of the sample do not move. Moreover, the tip wears less quickly. In practice, the frequency is fixed, close to the resonant frequency, away from the sample. Approaching it, the attractive and repulsive forces then modify the range of oscillation of the lever. Controlling this amplitude makes it possible to regulate the tip/sample distance and to constitute a topographic image. The main advantage of this intermittent mode is the virtual absence of lateral forces, and therefore very little wear on the tips and a greater diversity of measurable samples. Its major drawback is that the force exerted, admittedly reduced compared to the contact mode, is difficult to control.

2.2. Phase Imaging

Phase imaging allows mapping variations in surface properties of polymer materials due to the difference in terms of adhesion, friction and elasticity forces. This results in phase lag monitoring between the output signal and the cantilever oscillation (Figure 2). Changes in the phase lag result in a change in the physical properties on the sample surface [85]. Phase imaging, a method closely connected with IC-AFM, enables surface properties to be observed beyond pure topography. This results in a phase change as well as the lower amplitude of the cantilever oscillation. Since this phase change is a feature of the sample material's energy absorbency, it is characteristic for rigid or soft materials or, more generally, low and high-energy absorbency materials (Figure 2) [86].

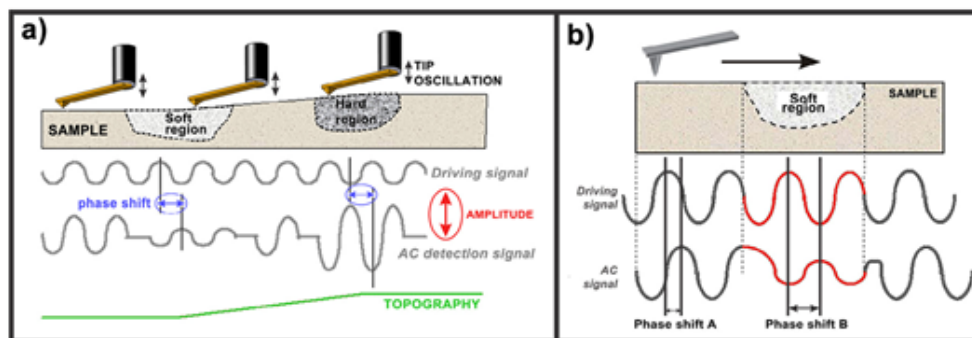


Figure 2. Lag changes due to the difference of mechanical properties of sample surface: (a) mode of modulation and (b) typical force curves [33,85]. *Reproduction with permission of Elsevier.*

Phase imaging enables the study of the dissemination of various materials or processes in the sample, e.g., phase differentiation among lipids [87] or drug delivery inside nanoparticles [88].

2.3. Atomic Force Microscopy

AFM can be used to determine the variation of the pressures between the AFM tip and the surface sample, thereby producing curves of force-distance [89]. A sort of forces can be spotted. These consist of van der Waals forces, Coulomb forces, electrostatic forces, or forces in ligand-receptor pairs [90–94]. As mentioned above, the principle of AFM is based on determining the forces between the tip of the AFM and the surface of the sample. Atomic Force Spectroscopy (AFS) has several advantages over other techniques such as: (i) the stylus profile meter that is the probe's high lateral positioning, enabling the sample's behavior to be observed at the nano-scale resolution, and (ii) high-sensitivity force, enabling forces to be recorded down to the pN range [95].

2.4. Cantilever-Tip Systems

One of the furthest essential tools to obtain images at the nanoscale is AFM that applies a cantilever with a sharp probe scanning on the sample surface. Hooke's law helps better understand the forces between the AFM tip and the sample surface where a laser beam senses the deflection. The cantilever can be supposed as a spring. The force between the sample surface and the AFM tip is related to the cantilever's spring constant (i.e., stiffness) as well as the distance between the tip and the surface [96].

Hooke's law [96]:

$$F = -k \cdot x \quad (2)$$

where F = force, k = spring constant, and x = cantilever deflection.

For high-resolution imaging by an AFM tip, its structure, radius and chemical composition are the key factors. The key limiting factor concerning an AFM's overall resolution is the tip apex radius. Highlights in the tip's size range are distortedly and extended, smaller highlights may not be apparent at all [97]. As the cantilever's spring constant is less than air, a folding of the cantilever happens, and this deflection is tracked [98].

The nanoprobe is often used as a metal-coated tip to have additional properties, such as conductivity, in scanning probe microscopes. However, this method is more costly because the specimens can be harmed by the diamond coatings [98]. New studies have developed prototypes of nanoprobe tips that are coated with different materials. For instance, Dai et al. [99] have developed a conventional scanning probe microscope (SPM) probe tips by adding multi-walled carbon nanotubes (with 1 μm and 5–20 nm diameter) to their apex using manual manipulation and optical microscope epoxy [100]. Many works [101–106] have shown that graphene can be a suitable coating material to extend the lifespan of a conductive nanoprobe. This prototype offers better mechanical durability with high conductivity without raising the tip radius and/or changing the spring constant of the cantilever. Its mass is minuscule compared to hard coatings like diamond that have a substantial mass. Graphene may also be used to functionalize the probe's surface with piezoelectricity and hydrophobicity properties [100].

The cantilever and the tip placed at its end are very important elements. Derived from complex microfabrication processes, there are different types, different shapes and composed of different materials. We will describe in this paragraph the type of lever/tip systems that we mainly used for our work. These are cantilevers formed of a rectangular silicon beam with an aluminum coating, on the upper part, to better reflect the laser spot. Depending on the dimensions of the lever, different stiffness values are available, modifying the pressing force exerted for a given deflection. We used levers with stiffnesses between 0.2 N/m and 40 N/m. The points integrated into these levers are of tetrahedral geometry

Microfabrication etching technique is one of the most commonly used methods for preparing AFM tips. The cantilever/sample systems are etched using this method from oxidized silicon wafers using photographic masks to describe the cantilever's form. This leads to tips with a radius below 30 nm. Super tips can be generated at the end of pyramidal Si_3N_4 tips through the regulated growth of carbon filaments (Figure 3) [107]. The tips developed by these techniques are later modified by surface yielding well-defined sensor systems at the nano-resolution to characterize the physicochemical, mechanical, and elastic properties of the sample. For example, nano-sensors can be produced by the covalent binding of DNA molecules based on a wide range of chemical reactions [108].

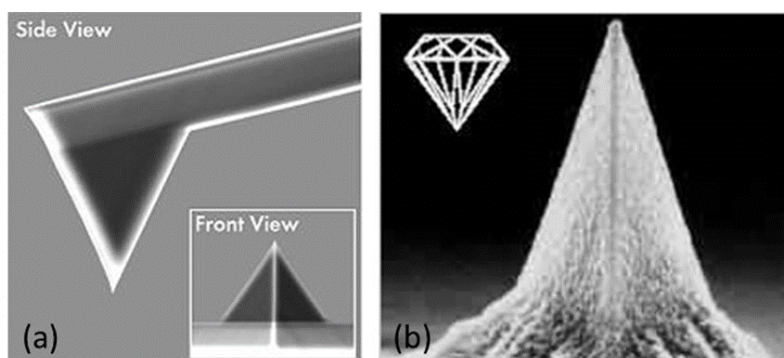


Figure 3. (a) AFM Si_3N_4 tip with Cantilever and (b) diamond coated AFM tip, adapted from [109].
Reproduction with permission of Nanomonde Co. (USA).

2.5. Principle of AFM-IR Technique

AFM-IR is a combination of an AFM and a tunable IR radiation to detect a photo-thermal effect and access chemical information down to a nanoscale resolution [110]. Through AFM-IR, the limit resolution of sub-diffraction is obtained. This is done via tracking the diversion of an AFM probe which is in contact with the sample surface and is deflected by rapid transient thermal expansion of the sample following of the absorbance of an infrared pulse. This has already been seen to associate well with measured infrared absorbance using traditional macroscopic FT-IR [111]. The principle of AFM-IR [112] is to couple the AFM in contact mode (or tapping mode) with a pulsed tunable laser is shown in Figure 4. In the first-generation AFM-IR, a sample is irradiated near field infrared radiations or laser through an infrared-transparent prism (ZnSe). The photo-thermal temperature of the sample increases when the wavelength of the laser diode is within the sample's absorption bands. The local rapid thermal expansion of the sample takes place as it heats up by absorbing radiation from the laser. The AFM cantilever senses this rapid thermal expansion of the sample through pulses that excite resonant oscillations. However, ring-down mechanisms can gradually decay these oscillations (Figure 4).

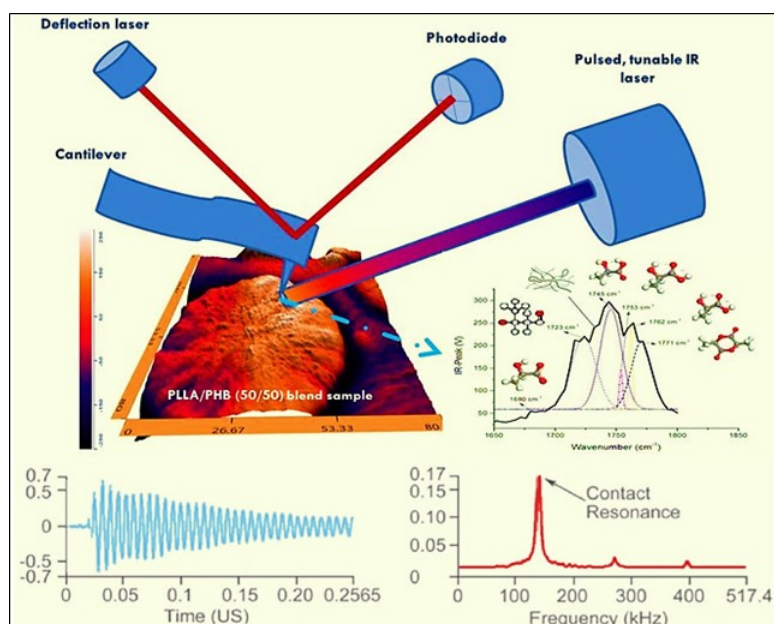


Figure 4. Principle of AFM-IR technique. Insert image shows an example of carbonyl groups of the blends of polyhydroxy butyrate and polylactide acid (50/50). *This figure is designed by the authors.*

Special data acquisition electronic systems measure the cantilever deflection concerning the laser pulses. By extracting the frequencies of the oscillations and amplitudes by Fourier techniques, the ring-down mechanisms can be studied. Local absorption FT-IR spectra, similar to standard transmission spectra, can result from the measurement of cantilever oscillations, which is dependent on the source wavelength. Besides, the oscillation frequencies of the ring-down determined using the Fourier techniques can also be used to qualitatively measure the sample's mechanical stiffness. The single wavelength of the IR source can determine the sample's mechanical properties and surface topography. The new AFM-IR system (nanoIR2) can also perform local thermal measurements of the surface of a sample. These measurements are done by bringing a probe capable of being heated in contact with the sample's surface. The probe is typically a microfabricated structure made of silicon with a sharp tip at the end of a long cantilever extending from a substrate. The sharp tip contacts the sample surface while the long cantilever allows sensitive force control between the tip and sample. The probe is resistively heated by flowing current through a conductive path in the cantilever. The system will automatically ramp the probe temperature and record the deflection of the probe along

with several other possible signals. The probe can be manually positioned at many locations or the system also has the capability using the Array function to measure the sample over an area on the sample's surface.

While in the top-down method, the advantages of scanning probe lithography are high-resolution molecular, chemical, and mechanical non-patterning capabilities, accurately controlled non-patterns are limited for high throughput applications and manufacturing. Although, the AFM allows analyzing samples with a spatial resolution order of 50–100 nm. In some cases, it will be impossible to prepare the sample with such a thin film (under 1 μm). For example, in the metal sector or silicon materials, it is very hard to prepare a thin film under 1 μm by using a microtome. To overcome this drawback, Baden et al. [113] adopted a new approach by using the focused ion beams (FIB) instead of the preparation of thin-film by a microtome. Although this method may lead to several deteriorations of the substrates due to the ion bombardment attacks and local thermal heating. However, the damages on the studied polymer surface (polyimide) by ion beam irradiation were negligible and the chemical structure of polyimide before and after treatment with FIB remains mostly unchanged. This kind of information is very interesting because it helps to overcome the drawbacks of this new technique at least with polyimide. The analysis of ultrafine particles (UFPs) needs higher sensibility equipment. For this purpose, a new resonance-enhanced method to increase the sensibility of AFM-IR by using the Lorentz contact resonance (LCR) imaging mode is proposed.

With this improvement, it is possible to perform nanoscale IR spectroscopy on extremely thin films to even 5 nm thick [55]. In other words, with the new devices, AFM-IR (models: NanoIR2s, NanoIR3, commercially available from Anasys Instruments Inc.) can be able to investigate single polymer lamellae, self-assembled monolayers and biological membranes. The responsivity of AFM-IR can be also improved by using a quantum cascade laser (QCL) [54,114]. To demonstrate a spatial resolution higher than 50 nm, it is necessary to tune the repetition rate of the QCL that can match AFM cantilever's one of the contact mode resonance frequencies. A spatial resolution of 25 nm has been reported to be achieved along with the sensitivity of self-assembled monolayers by using top-down illumination employing a gold-coated substrate and gold-coated AFM tip. The synchrotron IR beam in the resonance-enhanced AFM-IR configuration is amplitude modulated using a mechanical chopper. The mechanical chopper should be accustomed to a cantilever contact-resonance frequency. However, it should be noted that the interactions between the AFM tip and the sample surface determine the cantilever contact-resonance frequency. Noisy signals or complete loss of signals can emerge in the measurement if the resonance conditions are not properly maintained. Failure to correctly manage this resonance state may make larger noise levels in the calculation and/or lead to the total loss of signal [115].

Another mode is also used with AFM-IR, so-called the scanning thermal microscopy (SThM) mode. This is a mode where a special AFM tip scans the surface of the sample surface via the contact mode. This tip has a resistive element near its apex. As the tip changes temperature due to variations in the thermal conductivity or temperature of the sample in contact with the tip, the resistance of this element changes. This resistance change is monitored by the hardware using a Wheatstone bridge circuit and can be output to the controller to generate an image. To run experiments, you mount the sample onto a substrate, place it on the sample stage, and obtain an image of the sample's surface in the contact mode, following the normal AFM procedure but using a resistive thermal probe. Later, the user applies a voltage to the resistive thermal probe, balances the Wheatstone bridge and measures a voltage which is characteristic of the resistance of the probe. This voltage displayed along with the other images in the Analysis Studio software.

Surfaces of samples having sharp curvatures can concentrate the electromagnetic fields via the "lightning-rod effect" [116]. Such an effect improves the field confinement due to the sample surfaces sharp edges, which can provide increased sensitivity [117]. Recently, Dazzi et al. reported the AFM-IR using tapping mode, which complemented the AFM-IR's contact mode. This technique can be appropriate for samples with soft nature or loosely packed surfaces including polymeric

nanoparticles [118–120]. In the tapping mode, the cantilever oscillates vertically, near the resonance, which can reduce or eliminate the shear forces posing the risk of damage to the sample surface or the tip during scanning [121]. A spatial resolution of 10 nm for soft samples can be attained using the tapping AFM-IR technique with a heterodyne detection scheme [118,119].

2.6. Nano-Thermal Analysis (Nano-TA)

The other significant feature of AFM is about its attitude to be coupled with thermal analysis to better characterize the thermal properties of heterogeneous samples in different regions. Also recognized as nano-thermal analysis (nano-TA), this groundbreaking AFM-related method enables a local thermometric analysis [122]. This technique is often used to measure local thermal transitions of materials that can be imaged with AFM. A special thermal probe with capabilities to be heated under controlled conditions via the applied voltage is used for this analysis (Figure 5). The probe is subsequently relocated to the point of interest while increasing its temperature at the same time after imaging the sample surface. The temperature from the probe tends to locally heat the sample coming in contact with it. During this thermal ramping process, any deflection or resistance by the probe is recorded along with the power applied. Figure 5 illustrates the probe's initial upward deflection caused by the sample's thermal expansion followed by its penetration into the sample from the localized softening or melting of the sample's surface. This phenomenon occurs at the glass transition temperature or melting temperature of the sample due to a high resistance region of the probe (e.g., standard silicon probe).

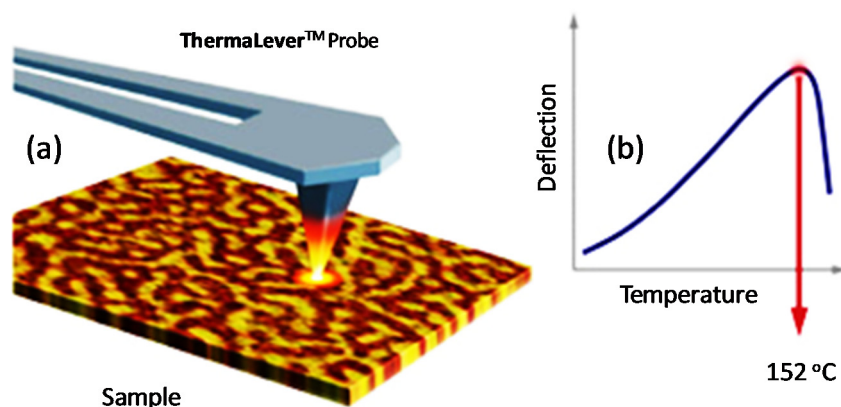


Figure 5. (a) Nano-TA uses a heated AFM tip to measure (b) thermal transition of polymer. *Reproduction with permission of Bruker Inc. [123].*

There are two styles of micromachined ThermoLever probes available. One has a cantilever length of $\sim 300\ \mu\text{m}$ and the other has a length of $\sim 200\ \mu\text{m}$. The ThermoLever probes have tip heights of 3–5 μm and a large area to reflect the AFM laser. The 300 μm cantilevers can achieve a maximum temperature typically of 400 $^{\circ}\text{C}$ and the 200 μm cantilevers achieve a maximum temperature of 350 $^{\circ}\text{C}$. Both styles of probes are made from doped Silicon which means that the temperature change with resistance is nonlinear. This means that when calibrating the probe temperature, three calibration samples are required to accurately calibrate the probe. Also, the probe will have a maximum temperature as mentioned above. This maximum temperature is the highest temperature that can be achieved before the resistance turnaround point.

The main advantage of testing nano-scale thermal analyzes is the detection of changes in the polymer crystal state, particularly the glass transition temperature (T_g) and melting temperature (T_m), without affecting its mechanical properties. During the measurements, the cantilever is heated while the probe is moved toward the specimen until its expansion due to the cantilever is local heating (Figure 5). The sample swelling pushes the probe up and causes a rise in the vertical bending of the cantilever. Therefore, this deflection is assessed by applying AFM photo-detector device based on

an AFM standard. The specimen changes its internal temperature due to the change in transition temperature at the softer state than the initial state. Hence, the cantilever bending decreases and the sample is forced to induce elastic or plastic deformation [122].

3. Application of Advanced AFM in the Crystallization of Polymers

3.1. AFM in Polymer Crystallization

3.1.1. Primary Stages of Crystallization

AFM is likely used to exclusively investigate the crystallization of polyolefin polymers at the nanoscale level [123–125], especially in the initial stages of crystallization. For example, the classical nucleation theory anticipated the development of ephemeral embryos in variable sizes. The embryos can grow, shrink, and probably stochastically disappear, but a Boltzmann distribution characterizes the overall population. This object only becomes a stable crystal nucleus as the critical size is attained by an embryo. At this stage, the transition-driving free energy offsets the surface energy [73]. In poly(bisphenol A octane ether) or PBA-C8 [126] and elastomeric PP, these germinations were recorded as transient dots [127]. Both the polymers gradually crystallize at room temperature, thus making in-situ observations easier.

When a stable nucleus is shaped, it is possible to follow in-situ growing and splitting of a “founding lamella” seen edge-on. Figure 6 shows the primary stage of nucleation followed by the initial growth of an edge-on founding lamella of PBA-C8 and its subsequent branching [128]. The growth phase and branching of poly(ethylene oxide) or PEO have also been reported by Schönherr [129]. The primary nucleation or spherulite formation occurs either homogeneously (as described above) or heterogeneously (with single lamella grown in the melt or primary nucleation from a preceding surface) [130]. For instance, 6 edge-on lamellae developing from a shared center can be found in the case of PBA-C8 [126,128].

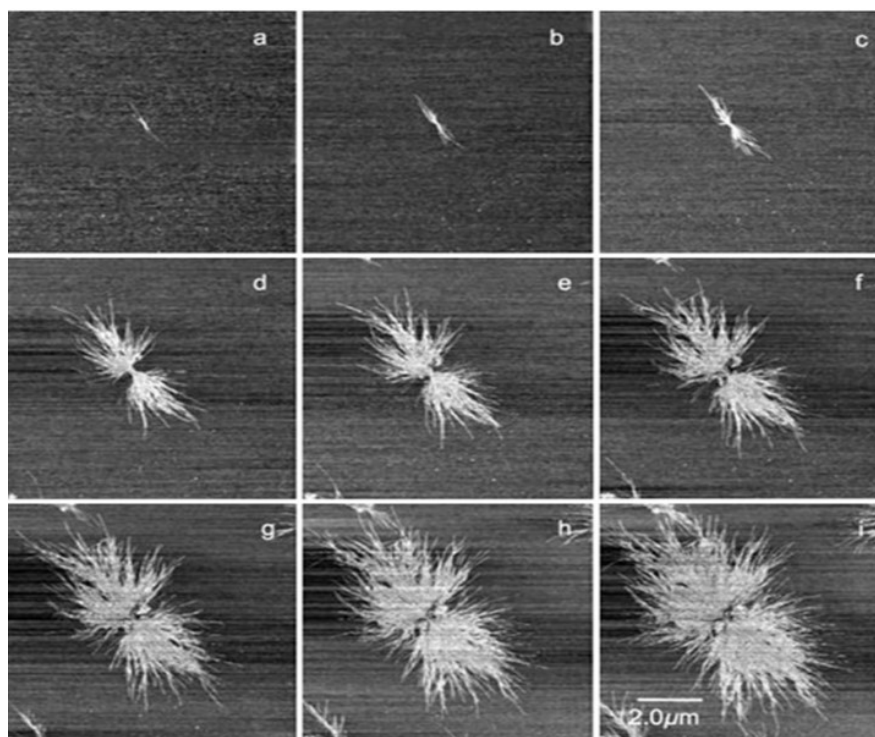


Figure 6. Phase images of spherulite development in PBA-C8 at different crystallization times: (a–i) The temperature was 30 °C and the overall time was 167 min. *Reproduction with permission of Elsevier [126,128].*

The typical mode of spherulite formation can be diagnosed mostly through single-angle splitting with the repetitive production of new lamella near and parallel to the newly formed lamella followed by their widening [131]. Although low-angle branching is an essential feature in the formation of spherulite, the dominant cause of such splitting is not universally agreed. Chan et al. [126] suggested that the non-crystallographic and low angle splitting of lamellar is caused by the induced nuclei. It is assumed that cilia or any unsecured folds on the basal surfaces of the parent lamella are organized as the embryonic crystals tied to the parent structure.

With a mean of roughly halfway between T_g and T_m , the temperature required to induce nucleation and lamellar growth is almost equivalent (Figure 6). Firstly, an induced nucleus appears as stable bright spots contiguous to the primary lamellae (Figure 6a–c), which further develop into secondary lamellae (Figure 6d–i).

3.1.2. Effects of Film Thickness

Investigations on constrained systems phase transitions and polymer crystallization in thin and ultra-thin films have gained interest due to AFM's popularity. Liu and Chen [132] wrote have extensively reviewed this subject, a few notable points are summarized here. Crystallization leads to edge-on oriented lamellae and growth rates are similar to those in bulk for molten thin films (thickness > 200 nm). For thin films with a thickness of 100–200 nm, a sudden transition is noticed from edge-on lamellae to face-on lamellae. The rate of growth of the well-studied isotactic polystyrene (iPS) system is $G(d) = G(1-ad-1)$ where “ $G(1-ad-1)$ ” is the bulk rate and the parameter “ $a = 6 \text{ nm}$ ” is insensitive to the crystallization temperature, substrate and molecular weight [133]. The reason for this slowdown in the ultra-thin film regime's crystallization rate is not recognized. A stronger dependence of $G(d)$ on $d-1$ for PEO grown on an attractive substratum has been reported. Once the thickness of the film exceeds the thickness of the lamellar $l_c \approx 10 \text{ nm}$, extra changes are seen. The reduced (thinner) melting regions around each growing crystal are observed here. $G(d)$ dependence on $d-1$ is reduced. As shown in Figure 7, the lamellae show that the growth morphology at any given temperature can be stiffer and flexible.

The diffusion length $\delta = DG^{-1}$ is a suitable parameter to realize some features of crystal morphology. In this case, D is the diffusivity [$\text{m}^2 \cdot \text{s}^{-1}$] of matter, mechanical, or thermal energy, which affects the crystallization. The extent of π is an indicator of the field immensity in front of the crystallization axis. It can be higher for slow growth rate undercooling (close to T_m) and smaller for rapid growth rate at lower T_c , where G is larger, and D is abridged. The rate of growth G is constant in time in all experiments considered here, maintaining consistency with the crystallization rate interface control. Furthermore, the morphology of the crystal can be influenced by the diffusion without imposing a dependency of $t^{-1/2}$ on the growth rate (G). The development of a smooth topological interface is unstable to local contour variations. Mullins-Sekerka instability can be explained by the development of fast-growing fingers and associated thin characteristics with a transverse size proportional to $(DG-1)^{1/2}$ [134].

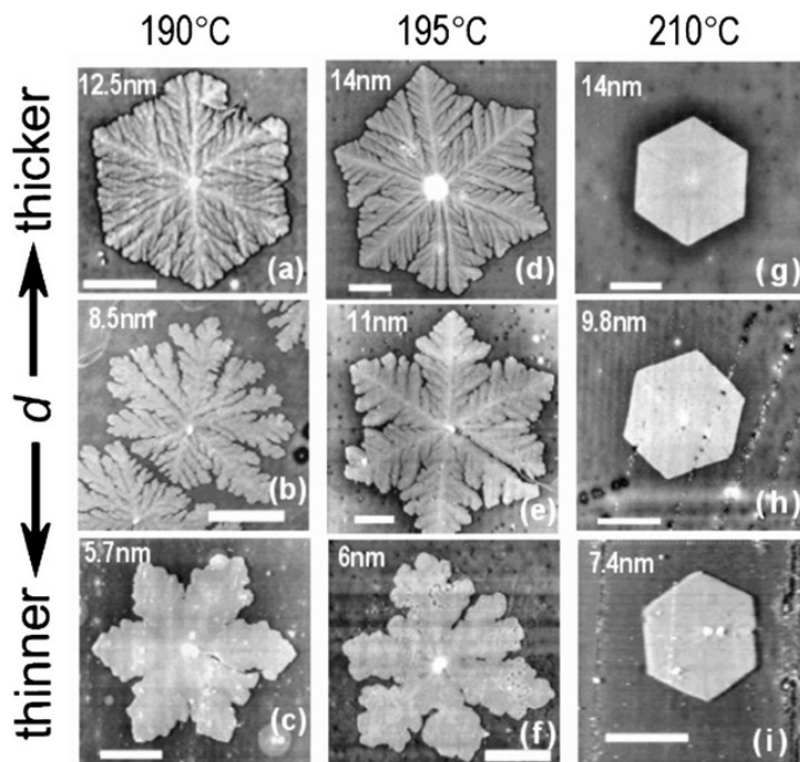


Figure 7. AFM images of crystals grown from ultrathin films of iPS at different temperatures and sample thicknesses. *Reproduction with copyright permission from Elsevier, Prud'homme R.E [135].*

With numerous potential advantages by combining a nanoscale morphological characterization and chemical composition identification, the AFM-IR is a worthwhile analytical tool for the chemical characterization of a variety of materials, especially for structure-property relationships. We describe here the latest progress in the application of this technique to identify, verify the miscibility, interaction, aging and crystallization of polymer, as well as related phenomena, which cannot be done with traditional AFM techniques [136]. Moreover, the information of these analyses is limited in the literature.

The direct visualization of primary nucleation at an early growth stage has been made possible through AFM imaging of polymer crystallization, which was previously unapproachable. The findings obtained through AFM have mostly complemented derivations from other methods or existing theory. However, several new questions have evolved, particularly concerning the understanding the branching caused by induced nucleation, operation of huge screw dislocations and the identification of polymer during crystallization.

3.2. AFM-IR in Polymers

3.2.1. Polymers Blends

For blend materials, the understanding direct determination of the miscibility, understanding polymeric separation and chemical interactions in a formulation are crucial to controlling the final properties. However, it remains key challenges due to the lack of correlated imaging tools at the sub-nanometer and chemical characterization. The first application of AFM-IR in polymer blends that should be mentioned was the work of Prater et al. [137] in which they tried to use AFM-IR to characterize a tertiary blend of common commercial polymers including polycarbonate (PC), epoxy resin (ER), polystyrene (PS). The AFM-IR technique can provide infrared spectra series in the C–H stretching region at different positions on the sample surface. The amplitude of the cantilever oscillation is related to the amount of infrared radiation absorbed by the sample [111,132–142].

The obtained results showed changes in terms of peak intensities of the C–H bonding in the spectral range of 2920–2970 cm^{-1} as the tip moved from PC to PS domains. Polycarbonate (PC)/Acrylonitrile butadiene styrene (ABS) blends are one of the most popular materials used in automotive and electronics devices. This is due to their excellent properties such as toughness, resistance to heat and ability for high flow during molding. AFM-IR can be used to explore the deflection of PC/ABS blends by setting the IR source to a constant wavenumber before scanning. The characterization and distribution of polymer in ABS/PC composite were performed by recording the nano-IR spectra in the C–H stretching region of 2800–3200 cm^{-1} . The aromatic C–H stretching vibration in polystyrene (PS) was found at the IR band of 3028 cm^{-1} . The CH_3 stretching band at 2960 cm^{-1} assigned to PC and CH_2 -stretching band at 2932 cm^{-1} attributed to polystyrene (PS) exhibit significant changes when the AFM cantilever scanned the sample surface to provide the chemical composition of ABS/PC at the nanoscale [143].

Felts et al. [140,144] have investigated several polymer systems, including polyethylene (PE), polystyrene (PS), and poly(3-dodecylthiophene-2,5-diyl) (PDDT), for their chemical characterization, nanoscale imaging and tip-based nanofabrication with spatial resolutions over 100 nm. The polymer nanostructures were written near a similar substrate, with some nanostructures overlapping. The position of absorption peaks at 2926 cm^{-1} was attributed to asymmetric C–H stretch. The band at 2860 cm^{-1} was assigned to symmetric C–H stretching. These peaks can shift to lower or the higher frequency with a variety of feature sizes. This is because of the thermal expansion of polymer blends, which depends on the feature size. Consequently, the cantilever response amplitude can lower with a decrease in the polymer feature size. In the case of PS and PDDT, although AFM-IR spectra show a low signal-to-noise, due to artifacts of laser power drift, the authors can still distinguish between nanostructures of polymers [145].

The determination of the miscibility of amorphous components in polymer blends used in pharmaceutical systems was also investigated by AFM-IR. Van Eerdenbrugh et al. [59,146] used AFM in combination with mid-IR spectroscopy to study the miscibility of an equimolar binary blend between poly-(vinylpyrrolidone) (PVP) with dextran or maltodextrin (DEX). By analyzing infrared absorption peaks at 1280 and 1350 cm^{-1} , the rich-DEX or rich-PVP domains were distinguished. More specifically, for pure DEX with a vibrational mode of (CH_2 wagging; CH_2 twisting) [147] and, the intensity of the band at 1350 cm^{-1} was higher than that of the 1280 cm^{-1} band, while for PVP with vibrational modes of C–H bend; CH_2 wagging, C–N stretch [148], the opposite tendency was observed. The AFM-IR results showed that the large discrete domains correspond to DEX-rich phases, while PVP enriches the continuous phase. The chemical and topographical images were in accordance.

In the petroleum and natural gas industry, the use of hydraulic fracturing techniques to crack rock is one of the most popular methods to release crude oil or natural gas by using sealing materials that can withstand ultra-high temperatures and high pressure (Ultra HTHP) [149]. These materials are often fabricated by a blend of high-performance materials including polytetrafluoroethylenes (PTFE), polyaryletherketones (PEEK), perfluoro-elastomers (FFKMs), and ethylene–propylene diene monomer (EPDM). A good understanding of the compatibility, the micro, nanostructure and the chemical properties of the blend is the key factor to improve their design and their process development. AFM-IR spectra helped chemical identification of each pure polymer component in the blend and thus can help to optimize the blending conditions [149]. AFM-IR spectroscopy and imaging can provide information for controlling the convergence of processing conditions to obtain a desirable mixing, which is ideal for a better performance of the end-use polymer [82].

Purohit et al. [58] investigated the miscibility of the drug-polymer amorphous solid dispersion (ASDs) of Itraconazole (ITZ) and hydroxypropylmethylcellulose (HPMC) blend through AFM-IR spectroscopy and fluorescence imaging. Both these techniques provided valuable information about ASDs microstructures. The ASD components underwent mixing upon the heating of the films. The authors affirmed that the AFM-IR is useful to characterize the microstructures in a drug-polymer system as well as their miscibility.

AFM-IR technique can help interpret the phase behavior of polymer blends that could be partially miscible such as poly(vinylpyrrolidone) (PVPK90) and hydroxypropyl methylcellulose acetate succinate (HPMCAS) to fabricate nanofibers for a tunable drug delivery system and nanoscale phase separation in electrospun blend fibers [150].

Recently, the miscibility of a polymer blend based on a pharmaceutical drug Telaprevir with three different polymers, an amorphous solid dispersion drug, was evaluated using nanoscale-IR spectroscopy, thermal analysis, and Lorentz contact resonance measurements [151]. The study indicated that AFM-IR is useful for phase separation and characterization of the microstructure of solid dispersion with respect to the polymer nature. According to the AFM-IR results, the continuous phase was enriched with polymer while the drug-rich phase formed discrete domains. These domains varied in size (from 50 nm to a few hundred) as a function of the system [151].

Tang et al. [57] used the AFM-IR technique on a commercial high-impact polypropylene to study the composition of its nano-domains. These consisted of mainly polypropylene along with some polyethylene (PE) and ethylene-propylene rubber (EPR) [57]. These materials possess multi-level phase structures and contain rubber particles in their core-shell with the dispersion of the internal structures in a continuous PP matrix with the order of several hundred nanometers as shown by AFM mapping images (Figure 8). The chemical characterization of this core-shell is impossible with a traditional FT-IR. Polypropylene (PP) exhibits a strong peak at about $1454\text{--}1457\text{ cm}^{-1}$ which is assigned to the vibration of a methylene group ($-\text{CH}_2$) in the PP side chains while both polyethylene (PE) and PP show a strong peak at the 1378 cm^{-1} band due to the vibration of symmetric bending of $-\text{CH}_2$ in the main chains. The AFM-IR spectra image at the 1456 cm^{-1} band (Figure 8b) helps to confirm the variation of PP concentration in such blend. In other words, by using the AFM-IR, they confirmed that the rigid cores consisted of mainly rubber particles of PP, not PE as previously described before. More recently, they published also a similar work on the use of both nano-TA and AFM-IR techniques to evaluate the chemical composition and structure of a high impact polypropylene (HIPP) [152]. Also, the principal component analysis (PCA) is one of the most significant and powerful techniques in chemometrics, besides in a wealth of other areas [153]. PCA is a method for decreasing the dimensionality of such datasets, increasing interpretability while minimizing information loss [154].

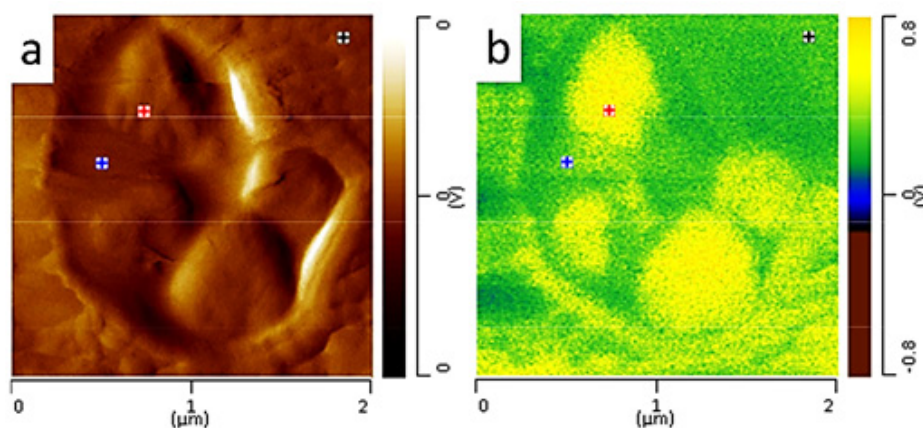


Figure 8. (a) AFM image and (b) AFM-IR image at the 1456 cm^{-1} showing the presence of polypropylene (PP) in the rubber nodules in a commercial high-impact polypropylene. *Reproduction with copyright permission from American Chemical Society, Tang et al. [57].*

3.2.2. Crystallization of Miscible Blends

The investigation on the distribution of polymer in miscible blends, especially on the sub-micrometer level is a practically difficult assignment despite the current advances in numerous X-ray techniques and microscopy [155–158]. AFM-IR has been used to examine the behavior of crystallization and diffusion in crystalline blends of poly(3-hydroxybutyrate) (PHB) and polyethylene

glycol (PEG). The addition of PEG helps to improve the biodegradation of PHB and extends its applications. However, the presence of PEG will perturb the crystallization of the PHB. By using the AFM-IR, it was possible to detect and derive a 3D polymer diffusion in this miscible blend by following the variation of the bands at 1095 cm^{-1} (C–OH stretching) observed in the PEG and 1720 cm^{-1} (C=O) found in PHB (Figure 9) [159].

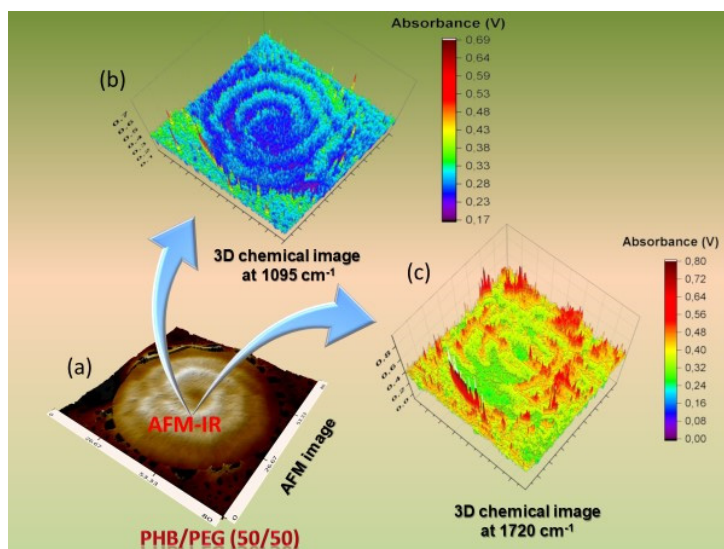


Figure 9. The PHB/PEG (50/50) blend isothermally crystallized at $40\text{ }^{\circ}\text{C}$: (a) tridimensional chemical image at the 1720 cm^{-1} band; (b) 3D AFM image and (c) 3D chemical image at the 1095 cm^{-1} band. Reproduced with copyright permission from American Chemical Society, Nguyen-Tri et al. [159].

3.2.3. AFM-IR in the Crystallization of Immiscible Blend

There are some works reported in the literature on the use of AFM-IR [160–163] to examine the behavior of polymer crystallization and diffusion in complex systems including equimolar miscible and immiscible crystalline blends at the nanoscale level [159,160,163]. Such studies used AFM-IR to analyze the crystallization behavior of an immiscible biopolyester based on polycaprolactone (PCL) and polyethylene glycol (PEG). The crystallization of this system is complex because they have a very similar melting temperature T_m and, thus, is expected to have simultaneous crystallization. However, the polymer phase separation at the nanoscale and the distribution of polymer in the sub-micrometer structure are limited. Thus, the mechanism of the crystallization process remains unexplored. The crystallization of an equimolar blend is first carried out at different temperatures between 30 and $40\text{ }^{\circ}\text{C}$ near the melting temperature and followed the technic of polarized optical microscopy (POM).

This demonstrates that, when the crystallization temperature goes lower than $37.5\text{ }^{\circ}\text{C}$, the crystallization has undergone in two steps. The first polymer crystallizes first to form spherulites and then suddenly, the nucleus of another polymer appears in the boundary of spherulites of the first polymer and grows perpendicularly to the interface. The crystals of the second polymer cannot develop to the spherulitic structure. When the temperature is higher than $37.5\text{ }^{\circ}\text{C}$, one step crystallization is observed. The transition from two steps to one step crystallization is perceived at $37.5\text{ }^{\circ}\text{C}$ where both inside and outside rejection are found. For the identification of the nature of each polymer in the blend, the AFM-IR spectrum of each pure component is first measured to determine the characteristic peak of each polymer. In this case, PCL exhibits a strong peak at about $1725\text{--}1728\text{ cm}^{-1}$ due to the presence of the carbonyl group, while this peak is absent in the PEG [160].

When the blend is quenched from the melt to an isothermal crystallization temperature of $40\text{ }^{\circ}\text{C}$, POM images show one-step crystallization of blend and the core-shell blended spherulites are not observed in this condition. Information about phase separation and the growth of PEG crystals are

ignored due to the resolution limits of POM. In several blends systems with a large difference of melting, POM equipped a hot stage that can be used to determine the identification and the distribution of polymer blend by heating overcome the melting of a polymer but lower than that of the other. The lower melting point polymer will be melted first and becomes darker under polarized optical microscopy observation. However, this destructive method is limited with blends having similar melting points like PEG and PCL.

AFM-IR is used to better understand the crystallization process of the PCL/PEG blends. High-resolution AFM images show a liquid-liquid phase separation without crystallization (Figure 10b). At the beginning of the crystallization, free energy from the supercooling process is not enough to cross over the energy barrier to form the stable nuclei and thus spinodal decomposition takes advantage of priority. With the crystallization time, in the PCL-rich domains starts to develop to nuclei and gathered together into spherulite-like features (Figure 10b). This structure continues to develop and occupy the entire sample surface including PEG rich regions. PEG-rich regions were blocked in the pre-existing PCL spherulites. The PEG rich areas nucleated and developed within PCL spherulite in confinement conditions. In this condition, the lamella density of PEG is lower than that of PCL and, thus, PEG crystals remain in the holes in the PCL template.

AFM-IR absorption maps of the carbonyl group of PCL at 1720 cm^{-1} can be used to examine approve these hypothesizes (Figure 10a,d). Figure 10a,d show a low IR absorption at 1724 cm^{-1} of small confined spherulites suggesting their main composition by PEG-rich domains. In contrast, IR absorption maps at 1092 cm^{-1} corresponding to the C–OH stretching in PEG represents a strong absorption in nodule structures. This allows confirming the PCL-rich domain belongs to bigger spherulites (c, f). The interface between two types of spherulites is also investigated by zooming in the small spherulite boundary at the sub-micrometers scale. Figure 10g–i represent the IR absorption AFM image map of the carbonyl group and IR absorption map of the C–OH group respectively. It can clearly distinguish two different regions containing PEG rich domains and PCL rich domains which are separated by spherulites boundary. It is very interesting to see that, in the PEG rich domains, there is also the presence of PEG lamella with the dimension of several tens of nanometers. This information is very interesting because, although because the blends are immiscible but the phase separation process during the cooling is not complete, the PEG is expected to be segregated into inter-lamella of PCL.

As acknowledged by the authors, for the first time, the distribution (or diffusion) of polymer in the blend can be directly observed at the nanoscale on a high-resolution AFM image. By using small-angle X-ray scattering (SAXS) and wide-angle X-ray scattering (WAXS) patterns, it is possible to speculate on lamellar structures in terms of their dimension, thickness and segregated mechanism. However, these analyses do not provide information on the morphology and direct observation of the lamella distribution in the blend at the nanoscale level. Full IR absorption spectra are also collected in PCL-rich domains (green and blue lines) and PEG rich domains (red and rose lines). It demonstrates that IR spectra are different from In the PCL rich regions and PEG rich domains. In the PEG-rich domain, there is a strong IR absorption band at 1092 cm^{-1} due to the C–OH stretching. However, the IR absorption intensity of this peak is weaker in the PCL region. In contrast, the IR absorption peaks at 1293 cm^{-1} , 1240 cm^{-1} , and 1190 cm^{-1} are attributed to the C–C stretching, C–O–C stretching and O–C–O stretching, respectively in the PCL regions.

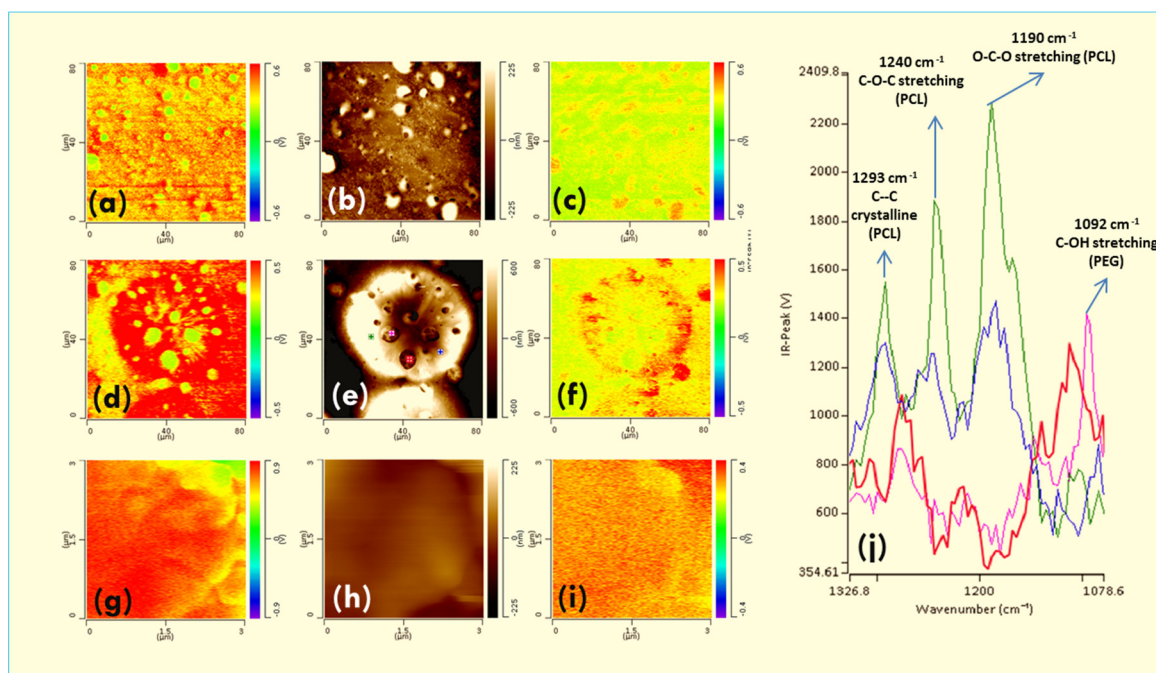


Figure 10. AFM images (b,e,h), IR mapping images (a,d,g) at 1724 cm^{-1} (carbonyl group of PCL), IR mapping images (c,f,i) and AFM-IR spectra (j) of PCL/PEG (50/50) blends isothermal crystallization at $40\text{ }^{\circ}\text{C}$. *Unpublished work.*

3.3. Other Applications of AFM-IR in Polymer Science

With numerous advantages of combining a nanoscale morphological characterization with chemical composition identification, the AFM-IR technique is found to be quite useful for a variety of materials. Some of the latest progress in the application of this technique to identify, verify the miscibility, interaction and aging, as well as related phenomena, which cannot be done with traditional AFM, are described here [55].

For composite materials, the chemical characterization in the interfacial region between polymer matrix and reinforcements is very important to better understand the final properties and the failure mechanisms during the service lifetime of polymeric materials. The latter may help formulations to converge more efficiently on optimal processing conditions. AFM-IR has shown to be a useful tool for this kind of analysis.

3.3.1. AFM-IR in Studying Polymer Aging

During the service lifetime the performance of polymers can deteriorate through the aging process due to environmental factors such as temperature, UV radiation and humidity [163–166]. This alteration can lead to the decommissioning of these products [167–171]. The aging of polymer material is manifested in physical and chemical degradations, a slow and irreversible process. The effects of this degradation resulting from the notion of the lifetime of the material, i.e., the time required a property (i.e., physical, chemical, or electrical) to reach a threshold below which the material becomes unusable. The term physical aging encompasses all processes leading to irreversible alteration of the material properties without a chemical modification of the structure of the macromolecules constituting the material. Physical aging [172] may result from the following: (i) changes in the spatial configuration of macromolecules (crystallization)-surface phenomenon; (ii) surface phenomenon (cracking of the surfactant environment); (iii) transport phenomenon (solvent penetration, migration of adjuvants).

Chemical aging [173] may relate from: (i) changes in the spatial configuration of macromolecules (crystallization)-surface phenomenon; (ii) surface phenomenon (cracking of the surfactant environment); and (iii) transport phenomenon (solvent penetration, migration of adjuvants). The main general types

of reactions involved in chemical aging are the following: scission of polymer chains, depolymerization, crosslinking, and oxidation. Understanding the aging mechanism is crucial because it can provide information on the prediction of the service lifetime of polymer materials. This can help to avoid accidents due to the use of unsuitable polymers and to interfere with the aging process to accelerate or slow down the degradation. In this direction, investigations on the aging and stability of polymers are extensively realized. The recent advances in nanoscale analysis have shed light on aging investigations. AFM-IR technique has also been used to better understand the aging mechanism of common polymers and composites.

Morsch's group has conducted several works on the use of AFM-IR technique to examine the aging processes of several coatings and polymers [174–178]. AFM-IR analyzed the chemical composition of aging products on the surface of a composite based on epoxy resin and silicon rubber. They used the electrical discharge to attack the composite surface and then investigate its effect on the chemical composition of the composite in the surface by both ATR-IR and AFM-IR. In many cases, ATR-IR gives similar results in aged and non-aged samples, meaning that the aging process does not affect the chemical structure of the composites. However, AFM-IR can provide more resolved spectra and nanoscale chemical mapping images of oxidative products (interfacial tracks and buried channels). The AFM-IR helps to confirm that the silicon rubber remains stable under these electrical attacks.

In another publication, both ATR-IR and AFM-IR techniques were used to investigate the degradation of oil paint used in the Picasso and Mondrian paintings [177]. The ancient painting made from linseed oil with inorganic titanium white pigment particles was analyzed to identify the degradation of these materials with time. The characterization of oxidative products on the painting surface is found to be very useful for better understanding the degradation mechanisms and thus can be said to be the best method for better preserving these artworks [177].

The aging mechanism of a PET fiber under accelerated aging conditions is also reported [161]. Although, PET is a common polyester polymer and the aging mechanisms of this polymer have been extensively investigated. However, there are still open questions relating to the distribution of oxidized functional groups on the fiber surface. The homogeneity of the polymer degradation on the surface at the nanoscale and molecular structure changes during the aging process of PET, as well as the degradation mechanisms [161,163,179,180]. Nguyen-Tri et al. have employed the AFM-IR technique to detect the distribution of functional groups at the surface of the PET fiber before and after aging tests [161]. They could able to propose a complementary mechanism for the PET under accelerated aging conditions. In another case, AFM-IR is used to compare the mechanism of aging of an organic coating based on polyurethane in two different conditions as follows [166]: (i) in natural exposure up to 10 years, and (ii) in accelerated conditions. They analyzed the distribution of carbonyl groups on the surface of both naturally and artificially aged samples. Two aging mechanisms were observed. In the naturally exposed coating, the oxidized group developed from holes and crack borders to the bulk matrix and this process is inhomogeneous, while in the accelerated aging condition, the oxidized groups are homogeneously distributed on the whole surface without serious crack on the sample surface. From the kinetic data on properties and structural changes, the authors have compared the results in both cases and proposed models to calculate the service lifetime of these coating.

3.3.2. AFM-IR in Biopolymers and Multilayers

Many bio-resourced based polymers have been synthesized or are formed in nature during the growth cycles of all organisms. The increase in the number of publications during recent years reflects the growing interest and importance of such new materials. The application of a new technique or method like AFM-IR to analyze morphology, properties and structure of these materials is attracting the more attention of the scientific community.

Mayet et al. [143] investigated the production of bacterial polyhydroxybutyrate in *Rhodobacter capsulatus* using TEM and AFM-IR. They concluded that AFM-IR was more useful and takes less time to prepare the sample compared to TEM. The samples can be ready for detailed analysis after 1 day

of preparation instead of 2–3 weeks for TEM analysis. The other advantages of AFM-IR relate to its capacity to obtain chemical images to directly ascertain the presence of PHB in blends by analyzing AFM maps at the 1740 cm^{-1} band (carbonyl group) which the TEM imaging could not do. AFM-IR was also used to study a laminated multilayer film interface based on ethylene acrylic acid (EAA) copolymer/polyamide (nylon) blend. Compared to traditional FT-IR having a special resolution of around $10\text{ }\mu\text{m}$, the use of AFM-IR shows better resolution at the interface. It was interesting to show that there was a very good correlation between the IR spectra of the polymer measured by bulk traditional FT-IR measurements and AFM-IR [55,171].

Gong et al. [56] used the AFM-IR technique to study the structure and morphology of individual biodegradable fibers (Figure 11). They indicated that the IR peak in AFM-IR complements well with the traditional FT-IR spectra in terms of the position of the peak and their relative intensity. The spectra obtained from AFM-IR are highly resolved that that obtained from the traditional FT-IR. By using AFM-IR combined with other characterization techniques such as wide-angle X-ray diffraction (WAXD) and selected area electron diffraction (SAED), a new mechanism of β -form crystal structures in the interface has been reported (Figure 11). Recently, Kelchtermans et al. [64] have employed the AFM-IR technique for the characterization of polyethylene-polyamide (PE-PA) multilayer films. They also confirmed that, in thin tie layers at the scale level, the analysis of the chemical composition was readily obtained.

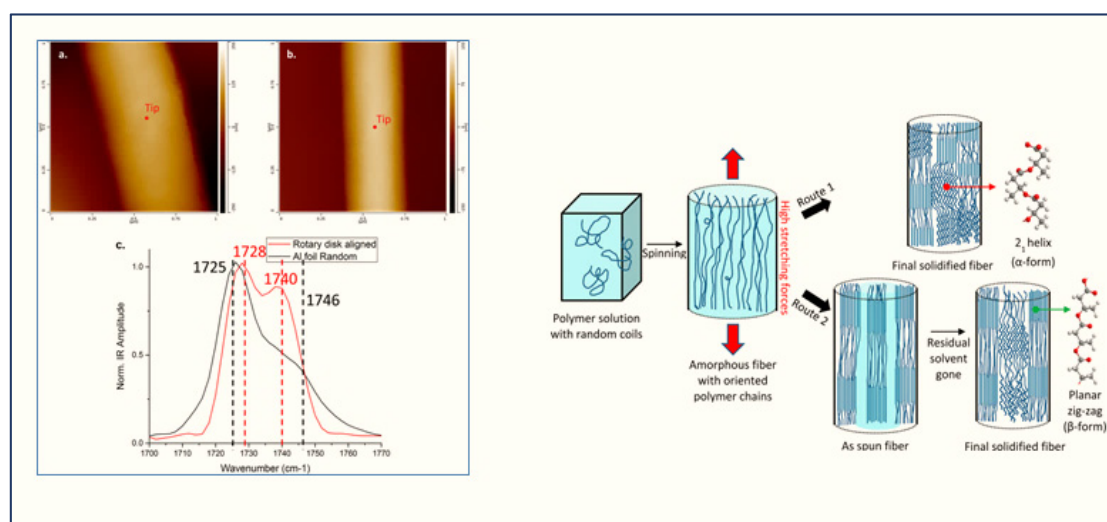


Figure 11. AFM-IR images and possible mechanisms for the formation of the α - and β -form crystal structure of single electrospun of PHBHx nanofibers. *Reproduced with copyright permission from Gong 2015 [56] (American Chemical Society).*

4. Summary and Outlooks

This paper provides the latest progress in the application of AFM-IR technique for polymer material studies dealing with polymer composites, polymer blends, biopolymers and multilayers. The paper demonstrated how this novel method can provide chemical information at the nanoscale scale based on the radiation absorption resulting from specific molecular vibrations. Secondly, we described the use of AFM and AFM-IR techniques to study the polymer crystallization in terms of the spherulite structure, lamella structure, and the distribution of polymer, by highlighting on two polymer blends of polyethylene glycol with polycaprolactone (PCL) (immiscible blend) and polyhydroxybutyrate (PHB) (miscible blend) at different scales ranging from inter-spherulite to inter-lamella. The paper discussed how AFM-IR can be used for investigating polymer aging and other systems including biopolymers and multilayer polymeric materials.

The recent applications found in the literature do not represent the real potential of this novel technique. It could certainly be applied in a broad range of research areas, including material science,

polymer, composites, blends, 3D printing, pharmaceuticals, biomedical and life sciences. In the polymer crystallization investigation, the improvement of the spatial resolution of AFM-IR up to 10 nm could bring various additional advantages in analyzing the chemical composition of complex blends, especially for thin and ultrathin polymeric films. The availability of new devices for AFM-IR in terms of laser source and sample heating/cooling system will be addressed to investigate the crystallization in situ a larger number of polymeric systems including tertiary or multiphase blends and helps to better understand the crystallization of complex and miscible polymer blends at the nanoscale.

Author Contributions: Conceptualization, P.N.-T.; resources, P.G., P.C., S.N., A.A.A., and D.D.N.; writing—original draft preparation, P.N.-T. and P.G.; writing—review and editing, P.N.-T.; supervision, P.N.-T.; project administration, P.N.-T.; funding acquisition, P.N.-T. All authors have read and agreed to the published version of the manuscript.

Funding: This research was funded by The Natural Sciences and Engineering Research Council of Canada (NSERC), grant number: DGECR-2020-00483.

Acknowledgments: We thank P. Moraille (University of Montreal, Canada) for her kind help in AFM-IR measurements. Thanks to Robert E. Prud'homme (University of Montreal) for his useful comments during the realization of this work.

Conflicts of Interest: The authors declare no conflict of interest. The funders had no role in the design of the study; in the collection, analyses, or interpretation of data; in the writing of the manuscript, or in the decision to publish the results.

References

1. Hobbs, J.K.; Farrance, O.E.; Kailas, L. How atomic force microscopy has contributed to our understanding of polymer crystallization. *Polymer* **2009**, *50*, 4281–4292. [[CrossRef](#)]
2. Koenig, J.L.; Wang, S.-Q.; Bhargava, R. Peer Reviewed: FTIR Images. *Anal. Chem.* **2001**, *73*, 360A–369A. [[CrossRef](#)] [[PubMed](#)]
3. Popescu, M.-C.; Filip, D.; Vasile, C.; Cruz, C.; Rueff, J.; Marcos, M.; Serrano, J.; Singurel, G. Characterization by Fourier transform infrared spectroscopy (FT-IR) and 2D IR correlation spectroscopy of PAMAM dendrimer. *J. Phys. Chem. B* **2006**, *110*, 14198–14211. [[CrossRef](#)] [[PubMed](#)]
4. Smith, P.A.M. Infrared microspectroscopy mapping studies of packaging materials: Experiment design and data profiling considerations. *Vib. Spectrosc.* **2000**, *24*, 47–62. [[CrossRef](#)]
5. Tannenbaum, R.; Zubris, M.; David, K.; Ciprari, D.; Jacob, K.; Jasiuk, I.; Dan, N. FTIR characterization of the reactive interface of cobalt oxide nanoparticles embedded in polymeric matrices. *J. Phys. Chem. B* **2006**, *110*, 2227–2232. [[CrossRef](#)]
6. Stelzer, E.H. Contrast, resolution, pixelation, dynamic range and signal-to-noise ratio: Fundamental limits to resolution in fluorescence light microscopy. *J. Microsc.* **1998**, *189*, 15–24. [[CrossRef](#)]
7. Lehmann, T.; Oberschelp, W.; Pelikan, E.; Repges, R. *Bildverarbeitung für die Medizin: Grundlagen, Modelle, Methoden, Anwendungen*; Springer: Berlin, Germany, 2013.
8. Nishikida, K. *Spatial Resolution in Infrared Microscopy and Imaging*; Application Note; Thermo Electron Corporation: Waltham, MA, USA, 2004; p. 50717.
9. Lasch, P.; Naumann, D. Spatial resolution in infrared microspectroscopic imaging of tissues. *Biochim. Biophys. Acta Bba Biomembr.* **2006**, *1758*, 814–829. [[CrossRef](#)]
10. Kumar, T.S. *Physical and Chemical Characterization of Biomaterials, in Characterization of Biomaterials*; Elsevier: Amsterdam, The Netherlands, 2013; pp. 11–47.
11. Ho, T.T.; Bremmell, K.E.; Krasowska, M.; MacWilliams, S.V.; Richard, C.I.J.; Stringer, D.N.; Beattie, D.A. In situ ATR FTIR spectroscopic study of the formation and hydration of a fucoidan/chitosan polyelectrolyte multilayer. *Langmuir* **2015**, *31*, 11249–11259. [[CrossRef](#)]
12. Tejedor-Tejedor, M.I.; Paredes, L.; Anderson, M.A. Evaluation of ATR—FTIR spectroscopy as an “in situ” tool for following the hydrolysis and condensation of alkoxy silanes under rich H₂O conditions. *Chem. Mater.* **1998**, *10*, 3410–3421. [[CrossRef](#)]
13. Roy, S.; Perez-Guaita, D.; Andrew, D.W.; Richards, J.S.; McNaughton, D.; Heraud, P.; Wood, B.R. Simultaneous ATR-FTIR based determination of malaria parasitemia, glucose and urea in whole blood dried onto a glass slide. *Anal. Chem.* **2017**, *89*, 5238–5245. [[CrossRef](#)]

14. Schuttlefield, J.D.; Grassian, V.H. ATR-FTIR spectroscopy in the undergraduate chemistry laboratory. Part I: Fundamentals and examples. *J. Chem. Educ.* **2008**, *85*, 279. [[CrossRef](#)]
15. Ami, D.; Mereghetti, P.; Foli, A.; Tasaki, M.; Milani, P.; Nuvolone, M.; Palladini, G.; Merlini, G.; Lavatelli, F.; Natalello, A. ATR-FTIR spectroscopy supported by multivariate analysis for the characterization of adipose tissue aspirates from patients affected by systemic amyloidosis. *Anal. Chem.* **2019**, *91*, 2894–2900. [[CrossRef](#)] [[PubMed](#)]
16. Maver, U.; Maver, T.; Peršin, Z.; Mozetič, M.; Vesel, A.; Gaberšček, M.; Stana-Kleinschek, K. Polymer characterization with the atomic force microscope. *Polym. Sci.* **2013**, *4*. [[CrossRef](#)]
17. Magonov, S. Atomic force microscopy in analysis of polymers. In *Encyclopedia of Analytical Chemistry: Applications, Theory and Instrumentation*; Wiley: Hoboken, NJ, USA, 2006.
18. Vahabi, S.; Salman, B.N.; Javanmard, A. Atomic force microscopy application in biological research: A review study. *Iran. J. Med Sci.* **2013**, *38*, 76.
19. Last, J.A.; Russell, P.; Nealey, P.F.; Murphy, C.J. The applications of atomic force microscopy to vision science. *Investig. Ophthalmol. Vis. Sci.* **2010**, *51*, 6083–6094. [[CrossRef](#)]
20. Stocker, W.; Schumacher, M.; Graff, S.; Thierry, A.; Wittmann, J.-C.; Lotz, B. Epitaxial crystallization and AFM investigation of a frustrated polymer structure: Isotactic poly (propylene), β phase. *Macromolecules* **1998**, *31*, 807–814. [[CrossRef](#)]
21. Hobbs, J.; Miles, M. Direct observation of polyethylene shish-kebab crystallization using in-situ atomic force microscopy. *Macromolecules* **2001**, *34*, 353–355. [[CrossRef](#)]
22. Hobbs, J.; Humphris, A.; Miles, M. In-situ atomic force microscopy of polyethylene crystallization. 1. crystallization from an oriented backbone. *Macromolecules* **2001**, *34*, 5508–5519. [[CrossRef](#)]
23. Ono, Y.; Kumaki, J. In situ real-time observation of polymer folded-chain crystallization by atomic force microscopy at the molecular level. *Macromolecules* **2018**, *51*, 7629–7636. [[CrossRef](#)]
24. Schulz, M.; Seidlitz, A.; Kurz, R.; Baärenwald, R.; Petzold, A.; Saalwachter, K.; Thurn-Albrecht, T. The Underestimated Effect of Intracrystalline Chain Dynamics on the Morphology and Stability of Semicrystalline Polymers. *Macromolecules* **2018**, *51*, 8377–8385. [[CrossRef](#)]
25. Sun, H.; Yu, D.M.; Shi, S.; Yuan, Q.; Fujinami, S.; Sun, X.; Wang, D.; Russell, T.P. Configurationally Constrained Crystallization of Brush Polymers with Poly (ethylene oxide) Side Chains. *Macromolecules* **2019**, *52*, 592–600. [[CrossRef](#)]
26. Boisseé, S.p.; Kryuchkov, M.A.; Tien, N.-D.; Bazuin, C.G.r.; Prud'homme, R.E. PLLA Crystallization in Linear AB and BAB Copolymers of L-Lactide and 2-Dimethylaminoethyl Methacrylate. *Macromolecules* **2016**, *49*, 6973–6986. [[CrossRef](#)]
27. Roland, S.b.; Gamys, C.G.; Grosrenaud, J.; Boisseé, S.p.; Pellerin, C.; Prud'homme, R.E.; Bazuin, C.G. Solvent Influence on thickness, composition, and morphology variation with dip-coating rate in supramolecular PS-b-P4VP thin films. *Macromolecules* **2015**, *48*, 4823–4834. [[CrossRef](#)]
28. Mareau, V.H.; Prud'Homme, R.E. In-situ hot stage atomic force microscopy study of poly (ϵ -caprolactone) crystal growth in ultrathin films. *Macromolecules* **2005**, *38*, 398–408. [[CrossRef](#)]
29. Maillard, D.; Prud'Homme, R.E. Crystallization of ultrathin films of polylactides: From chain chirality to lamella curvature and twisting. *Macromolecules* **2008**, *41*, 1705–1712. [[CrossRef](#)]
30. Vielmuth, F.; Spindler, V.; Waschke, J. Atomic force microscopy provides new mechanistic insights into the pathogenesis of pemphigus. *Front. Immunol.* **2018**, *9*, 485. [[CrossRef](#)]
31. Baker, A.; Helbert, W.; Sugiyama, J.; Miles, M. New insight into cellulose structure by atomic force microscopy shows the I α crystal phase at near-atomic resolution. *Biophys. J.* **2000**, *79*, 1139–1145. [[CrossRef](#)]
32. Dufrière, Y.F. Atomic force microscopy in microbiology: New structural and functional insights into the microbial cell surface. *MBio* **2014**, *5*, e01363-14. [[CrossRef](#)]
33. Maver, U.; Velnar, T.; Gaberšček, M.; Planinšek, O.; Finšgar, M. Recent progressive use of atomic force microscopy in biomedical applications. *Trac Trends Anal. Chem.* **2016**, *80*, 96–111. [[CrossRef](#)]
34. Edwardson, J.M.; Henderson, R.M. Atomic force microscopy and drug discovery. *Drug Discov. Today* **2004**, *9*, 64–71. [[CrossRef](#)]
35. Senapati, S.; Lindsay, S. Recent progress in molecular recognition imaging using atomic force microscopy. *Acc. Chem. Res.* **2016**, *49*, 503–510. [[CrossRef](#)] [[PubMed](#)]

36. Soon, R.L.; Nation, R.L.; Hartley, P.G.; Larson, I.; Li, J. Atomic force microscopy investigation of the morphology and topography of colistin-heteroresistant *Acinetobacter baumannii* strains as a function of growth phase and in response to colistin treatment. *Antimicrob. Agents Chemother.* **2009**, *53*, 4979–4986. [[CrossRef](#)] [[PubMed](#)]
37. Shan, Y.; Wang, H. The structure and function of cell membranes examined by atomic force microscopy and single-molecule force spectroscopy. *Chem. Soc. Rev.* **2015**, *44*, 3617–3638. [[CrossRef](#)] [[PubMed](#)]
38. Marrese, M.; Guarino, V.; Ambrosio, L. Atomic force microscopy: A powerful tool to address scaffold design in tissue engineering. *J. Funct. Biomater.* **2017**, *8*, 7. [[CrossRef](#)]
39. Frisbie, C.D.; Rozsnyai, L.F.; Noy, A.; Wrighton, M.S.; Lieber, C.M. Functional group imaging by chemical force microscopy. *Science* **1994**, *265*, 2071–2074. [[CrossRef](#)]
40. Piner, R.D.; Mirkin, C.A. Effect of water on lateral force microscopy in air. *Langmuir* **1997**, *13*, 6864–6868. [[CrossRef](#)]
41. Davis, J.J. *Engineering the Bioelectronic Interface: Applications to Analyte Biosensing and Protein Detection*; Royal Society of Chemistry: London, UK, 2009.
42. Smith, D.; Connell, S.; Robinson, C.; Kirkham, J. Chemical force microscopy: Applications in surface characterisation of natural hydroxyapatite. *Anal. Chim. Acta* **2003**, *479*, 39–57. [[CrossRef](#)]
43. Steffens, C.; Leite, F.L.; Bueno, C.C.; Manzoli, A.; Herrmann, P.S.D.P. Atomic force microscopy as a tool applied to nano/biosensors. *Sensors* **2012**, *12*, 8278–8300. [[CrossRef](#)]
44. Jarzemski, A.; Shaskey, C.; Park, K. Tip-based vibrational spectroscopy for nanoscale analysis of emerging energy materials. *Front. Energy* **2018**, *12*, 43–71. [[CrossRef](#)]
45. Liu, Y.; Collins, L.; Proksch, R.; Kim, S.; Watson, B.R.; Doughty, B.; Calhoun, T.R.; Ahmadi, M.; Ievlev, A.V.; Jesse, S. Chemical nature of ferroelastic twin domains in CH₃ NH₃ PbI₃ perovskite. *Nat. Mater.* **2018**, *17*, 1013–1019. [[CrossRef](#)]
46. Yang, J.; Hatcherian, J.; Hackley, P.C.; Pomerantz, A.E. Nanoscale geochemical and geomechanical characterization of organic matter in shale. *Nat. Commun.* **2017**, *8*, 1–9. [[CrossRef](#)] [[PubMed](#)]
47. Jin, M.; Lu, F.; Belkin, M.A. High-sensitivity infrared vibrational nanospectroscopy in water. *Light: Sci. Appl.* **2017**, *6*, e17096. [[CrossRef](#)]
48. Hassenkam, T.; Andersson, M.; Dalby, K.; Mackenzie, D.; Rosing, M. Elements of Eoarchean life trapped in mineral inclusions. *Nature* **2017**, *548*, 78–81. [[CrossRef](#)] [[PubMed](#)]
49. Qin, N.; Zhang, S.; Jiang, J.; Corder, S.G.; Qian, Z.; Zhou, Z.; Lee, W.; Liu, K.; Wang, X.; Li, X.; et al. Nanoscale probing of electron-regulated structural transitions in silk proteins by near-field IR imaging and nano-spectroscopy. *Nat. Commun.* **2016**, *7*, 1–8. [[CrossRef](#)] [[PubMed](#)]
50. Khanikaev, A.B.; Arju, N.; Fan, Z.; Purtseladze, D.; Lu, F.; Lee, J.; Sarriguarte, P.; Schnell, M.; Hillenbrand, R.; Belkin, M. Experimental demonstration of the microscopic origin of circular dichroism in two-dimensional metamaterials. *Nat. Commun.* **2016**, *7*, 1–8. [[CrossRef](#)] [[PubMed](#)]
51. O'callahan, B.T.; Jones, A.C.; Park, J.H.; Cobden, D.H.; Atkin, J.M.; Raschke, M.B. Inhomogeneity of the ultrafast insulator-to-metal transition dynamics of VO₂. *Nat. Commun.* **2015**, *6*, 1–8. [[CrossRef](#)]
52. Ruggeri, F.; Longo, G.; Faggiano, S.; Lipiec, E.; Pastore, A.; Dietler, G. Infrared nanospectroscopy characterization of oligomeric and fibrillar aggregates during amyloid formation. *Nat. Commun.* **2015**, *6*, 1–9. [[CrossRef](#)]
53. Ghosh, S.; Kouamé, N.A.; Ramos, L.; Remita, S.; Dazzi, A.; Deniset-Besseau, A.; Beaunier, P.; Goubard, F.; Aubert, P.-H.; Remita, H. Conducting polymer nanostructures for photocatalysis under visible light. *Nat. Mater.* **2015**, *14*, 505–511. [[CrossRef](#)]
54. Lu, F.; Jin, M.; Belkin, M.A. Tip-enhanced infrared nanospectroscopy via molecular expansion force detection. *Nat. Photonics* **2014**, *8*, 307. [[CrossRef](#)]
55. Dazzi, A.; Prater, C.B. AFM-IR: Technology and applications in nanoscale infrared spectroscopy and chemical imaging. *Chem. Rev.* **2017**, *117*, 5146–5173. [[CrossRef](#)]
56. Gong, L.; Chase, D.B.; Noda, I.; Liu, J.; Martin, D.C.; Ni, C.; Rabolt, J.F. Discovery of β -form crystal structure in electrospun poly [(R)-3-hydroxybutyrate-co-(R)-3-hydroxyhexanoate](PHBHx) nanofibers: From fiber mats to single fibers. *Macromolecules* **2015**, *48*, 6197–6205. [[CrossRef](#)]
57. Tang, F.; Bao, P.; Su, Z. Analysis of nanodomain composition in high-impact polypropylene by atomic force microscopy-infrared. *Anal. Chem.* **2016**, *88*, 4926–4930. [[CrossRef](#)] [[PubMed](#)]

58. Purohit, H.S.; Taylor, L.S. Miscibility of itraconazole–hydroxypropyl methylcellulose blends: Insights with high resolution analytical methodologies. *Mol. Pharm.* **2015**, *12*, 4542–4553. [[CrossRef](#)] [[PubMed](#)]
59. Van Eerdenbrugh, B.; Lo, M.; Kjoller, K.; Marcott, C.; Taylor, L.S. Nanoscale mid-infrared evaluation of the miscibility behavior of blends of dextran or maltodextrin with poly (vinylpyrrolidone). *Mol. Pharm.* **2012**, *9*, 1459–1469. [[CrossRef](#)] [[PubMed](#)]
60. Ma, X.; Zhou, X.; Yu, A.; Zhao, W.; Zhang, W.; Zhang, S.; Wei, L.; Cook, D.J.; Roy, A. Functionalized metal-organic framework nanocomposites for dispersive solid phase extraction and enantioselective capture of chiral drug intermediates. *J. Chromatograph. A* **2018**, *1537*, 1–9. [[CrossRef](#)] [[PubMed](#)]
61. Mikhanchan, A.; Banas, A.M.; Banas, K.; Borkowska, A.M.; Nowakowski, M.; Breese, M.B.; Kwiatek, W.M.; Paluszkiwicz, C.; Tay, T.E. Revealing chemical heterogeneity of CNT fiber nanocomposites via nanoscale chemical imaging. *Chem. Mater.* **2018**, *30*, 1856–1864. [[CrossRef](#)]
62. Ali, A.; Morrow, P.; Henda, R.; Fagerberg, R. Deposition of cobalt doped zinc oxide thin film nano-composites via pulsed electron beam ablation. *Mrs Adv.* **2016**, *1*, 433–439. [[CrossRef](#)]
63. Van Assche, G.; Van Mele, B. Interphase formation in model composites studied by micro-thermal analysis. *Polymer* **2002**, *43*, 4605–4610. [[CrossRef](#)]
64. Kelchtermans, M.; Lo, M.; Dillon, E.; Kjoller, K.; Marcott, C. Characterization of a polyethylene–polyamide multilayer film using nanoscale infrared spectroscopy and imaging. *Vib. Spectrosc.* **2016**, *82*, 10–15. [[CrossRef](#)]
65. Hinrichs, K.; Shaykhutdinov, T. Polarization-Dependent Atomic Force Microscopy–Infrared Spectroscopy (AFM-IR): Infrared Nanopolarimetric Analysis of Structure and Anisotropy of Thin Films and Surfaces. *Appl. Spectrosc.* **2018**, *72*, 817–832. [[CrossRef](#)]
66. Wang, H.; Wang, C.-T.; Xu, F.; Yang, J.; Liu, J.; Cai, W.; Zhu, G. Resistive switching and nanoscale chemical mapping of phase separation in PVDF/PMMA/F8T2 ternary thin films. *Polymer* **2018**, *153*, 498–506. [[CrossRef](#)]
67. Pancani, E.; Mathurin, J.; Bilent, S.; Bernet-Camard, M.F.; Dazzi, A.; Deniset-Besseau, A.; Gref, R. High-Resolution Label-Free Detection of Biocompatible Polymeric Nanoparticles in Cells. *Part. Part. Syst. Charact.* **2018**, *35*, 1700457. [[CrossRef](#)]
68. Perez-Guaita, D.; Kochan, K.; Batty, M.; Doerig, C.; Garcia-Bustos, J.; Espinoza, S.; McNaughton, D.; Heraud, P.; Wood, B.R. Multispectral atomic force microscopy-infrared nano-imaging of malaria infected red blood cells. *Anal. Chem.* **2018**, *90*, 3140–3148. [[CrossRef](#)] [[PubMed](#)]
69. Shaykhutdinov, T.; Pop, S.D.; Furchner, A.; Hinrichs, K. Supramolecular orientation in anisotropic assemblies by infrared nanopolarimetry. *ACS Macro Lett.* **2017**, *6*, 598–602. [[CrossRef](#)]
70. Centrone, A. Infrared imaging and spectroscopy beyond the diffraction limit. *Annu. Rev. Anal. Chem.* **2015**, *8*, 101–126. [[CrossRef](#)]
71. Fu, W.; Zhang, W. Hybrid AFM for nanoscale physicochemical characterization: Recent development and emerging applications. *Small* **2017**, *13*, 1603525. [[CrossRef](#)]
72. Xiao, L.; Schultz, Z.D. Spectroscopic imaging at the nanoscale: Technologies and recent applications. *Anal. Chem.* **2018**, *90*, 440–458. [[CrossRef](#)]
73. Crist, B.; Schultz, J.M. Atomic Force Microscopy Studies of Polymer Crystals: Nucleation, Growth, Annealing, and Melting. In *Encyclopedia of Polymers and Composites*; Palsule, S., Ed.; Springer: Berlin/Heidelberg, Germany, 2013; pp. 1–25.
74. Zhu, D.; Shou, X.; Liu, Y.; Chen, E.; Cheng, S.Z. AFM-tip-induced crystallization of poly (ethylene oxide) melt droplets. *Front. Chem. China* **2007**, *2*, 174–177. [[CrossRef](#)]
75. Magonov, S.N.; Reneker, D.H. Characterization of polymer surfaces with atomic force microscopy. *Annu. Rev. Mater. Sci.* **1997**, *27*, 175–222. [[CrossRef](#)]
76. Klinov, D.; Magonov, S. True molecular resolution in tapping-mode atomic force microscopy with high-resolution probes. *Appl. Phys. Lett.* **2004**, *84*, 2697–2699. [[CrossRef](#)]
77. Pearce, R.; Vancso, G.J. Real-time imaging of melting and crystallization in poly (ethylene oxide) by atomic force microscopy. *Polymer* **1998**, *39*, 1237–1242. [[CrossRef](#)]
78. Pearce, R.; Vancso, G.J. Imaging of melting and crystallization of poly (ethylene oxide) in real-time by hot-stage atomic force microscopy. *Macromolecules* **1997**, *30*, 5843–5848. [[CrossRef](#)]
79. McMaster, T.; Hobbs, J.; Barham, P.; Miles, M. AFM study of in situ real time polymer crystallization and spherulite structure. *Probe Microsc.* **1997**, *1*, 43–56.
80. Hobbs, J.K.; McMaster, T.J.; Miles, M.J.; Barham, P.J. Direct observations of the growth of spherulites of poly (hydroxybutyrate-co-valerate) using atomic force microscopy. *Polymer* **1998**, *39*, 2437–2446. [[CrossRef](#)]

81. Braga, P.C.; Ricci, D. *Atomic Force Microscopy: Biomedical Methods and Applications*; Springer Science & Business Media: Berlin, Germany, 2004; Volume 242.
82. Eaton, P.; West, P. *Atomic Force Microscopy*; Oxford University Press: Oxford, UK, 2009; ISBN-13: 978-0199570454.
83. Jagtap, R.; Ambre, A. Overview literature on atomic force microscopy (AFM): Basics and its important applications for polymer characterization. *Indian J. Eng. Mater. Sci.* **2006**, *13*, 368–384.
84. MikroMasch, N.G. Contact Mode, Ambient Conditions. Available online: <https://www.spmtips.com/how-to-choose-by-AFM-technique-contact-mode.html> (accessed on 10 April 2020).
85. Park Systems. Phase Imaging/Phase Detection Microscopy. 2020. Available online: <https://parksystems.com/park-spm-modes/91-standard-imaging-mode/221-phase-imaging-phase-detection-microscopy-pdm> (accessed on 10 April 2020).
86. Schmitz, I.; Schreiner, M.; Friedbacher, G.; Grasserbauer, M. Phase imaging as an extension to tapping mode AFM for the identification of material properties on humidity-sensitive surfaces. *Appl. Surf. Sci.* **1997**, *115*, 190–198. [[CrossRef](#)]
87. Lin, W.-C.; Blanchette, C.D.; Ratto, T.V.; Longo, M.L. Lipid asymmetry in DLPC/DSPC-supported lipid bilayers: A combined AFM and fluorescence microscopy study. *Biophys. J.* **2006**, *90*, 228–237. [[CrossRef](#)]
88. Simon, M.; Wittmar, M.; Bakowsky, U.; Kissel, T. Self-assembling nanocomplexes from insulin and water-soluble branched polyesters, poly [(vinyl-3-(diethylamino)-propylcarbamate-co-(vinyl acetate)-co-(vinyl alcohol)]-graft-poly (l-lactic acid): A novel carrier for transmucosal delivery of peptides. *Bioconjugate Chem.* **2004**, *15*, 841–849. [[CrossRef](#)]
89. Butt, H.-J.; Cappella, B.; Kappl, M. Force measurements with the atomic force microscope: Technique, interpretation and applications. *Surf. Sci. Rep.* **2005**, *59*, 1–152. [[CrossRef](#)]
90. Wong, J.; Chilkoti, A.; Moy, V.T. Direct force measurements of the streptavidin–biotin interaction. *Biomol. Eng.* **1999**, *16*, 45–55. [[CrossRef](#)]
91. Radmacher, M.; Cleveland, J.P.; Fritz, M.; Hansma, H.G.; Hansma, P.K. Mapping interaction forces with the atomic force microscope. *Biophys. J.* **1994**, *66*, 2159–2165. [[CrossRef](#)]
92. Quist, A.P.; Bergman, A.A.; Reimann, C.T.; Oscarsson, S.O.; Sundqvist, B. Imaging of single antigens, antibodies, and specific immunocomplex formation by scanning force microscopy. *Scanning Microsc.* **1995**, *9*, 395–400. [[PubMed](#)]
93. Florin, E.-L.; Moy, V.T.; Gaub, H.E. Adhesion forces between individual ligand-receptor pairs. *Science* **1994**, *264*, 415–417. [[CrossRef](#)] [[PubMed](#)]
94. Chen, A.; Moy, V.T. Cross-linking of cell surface receptors enhances cooperativity of molecular adhesion. *Biophys. J.* **2000**, *78*, 2814–2820. [[CrossRef](#)]
95. Rimondini, L.; Bianchi, C.L.; Vernè, E. *Surface Tailoring of Inorganic Materials for Biomedical Applications*; Bentham Science Publishers: Sharjah, UAE, 2012.
96. MicroscopeMaster. The Atomic Force Microscope (AFM): What Are Its Uses in Microscopy Today? Advantages and Disadvantages. 2020. Available online: <https://www.microscopemaster.com/atomic-force-microscope.html> (accessed on 10 April 2020).
97. Villarrubia, J.S. Morphological estimation of tip geometry for scanned probe microscopy. *Surf. Sci.* **1994**, *321*, 287–300. [[CrossRef](#)]
98. Wilson, R.A.; Bullen, H.A. Basic Theory Atomic Force Microscopy (AFM), Department of Chemistry, Northern Kentucky University. Available online: <Users.metu.edu.tr> (accessed on 10 April 2020).
99. Dai, H.; Hafner, J.H.; Rinzler, A.G.; Colbert, D.T.; Smalley, R.E. Nanotubes as nanoprobe in scanning probe microscopy. *Nature* **1996**, *384*, 147–150. [[CrossRef](#)]
100. Hui, F.; Chen, S.; Liang, X.; Yuan, B.; Jing, X.; Shi, Y.; Lanza, M. Graphene Coated Nanoprobes: A Review. *Crystals* **2017**, *7*, 269. [[CrossRef](#)]
101. Wen, Y.; Chen, J.; Guo, Y.; Wu, B.; Yu, G.; Liu, Y. Multilayer graphene-coated atomic force microscopy tips for molecular junctions. *Adv. Mater.* **2012**, *24*, 3482–3485. [[CrossRef](#)]
102. Lanza, M.; Bayerl, A.; Gao, T.; Porti, M.; Nafria, M.; Jing, G.; Zhang, Y.; Liu, Z.; Duan, H. Graphene-Coated Atomic Force Microscope Tips for Reliable Nanoscale Electrical Characterization. *Adv. Mater.* **2013**, *25*, 1440–1444. [[CrossRef](#)]
103. Shim, W.; Brown, K.A.; Zhou, X.; Rasin, B.; Liao, X.; Mirkin, C.A. Multifunctional cantilever-free scanning probe arrays coated with multilayer graphene. *Proc. Natl. Acad. Sci. USA* **2012**, *109*, 18312–18317. [[CrossRef](#)]

104. Martin-Olmos, C.; Rasool, H.I.; Weiller, B.H.; Gimzewski, J.K. Graphene MEMS: AFM probe performance improvement. *ACS Nano* **2013**, *7*, 4164–4170. [[CrossRef](#)] [[PubMed](#)]
105. Pacios, M.; Hosseini, P.; Fan, Y.; He, Z.; Krause, O.; Hutchison, J.; Warner, J.H.; Bhaskaran, H. Direct manufacturing of ultrathin graphite on three-dimensional nanoscale features. *Sci. Rep.* **2016**, *6*, 22700. [[CrossRef](#)] [[PubMed](#)]
106. Hui, F.; Vajha, P.; Shi, Y.; Ji, Y.; Duan, H.; Padovani, A.; Larcher, L.; Li, X.R.; Xu, J.J.; Lanza, M. Moving graphene devices from lab to market: Advanced graphene-coated nanoprobe. *Nanoscale* **2016**, *8*, 8466–8473. [[CrossRef](#)]
107. Keller, D.J.; Chih-Chung, C. Imaging steep, high structures by scanning force microscopy with electron beam deposited tips. *Surf. Sci.* **1992**, *268*, 333–339. [[CrossRef](#)]
108. Micic, M.; Chen, A.; Leblanc, R.M.; Moy, V.T. Scanning electron microscopy studies of protein-functionalized atomic force microscopy cantilever tips. *Scanning* **1999**, *21*, 394–397. [[CrossRef](#)]
109. NanoWorld AG. a) AFM Si₃N₄ Tip with Cantilever and d) Diamond Coated AFM Tip. Available online: <https://www.nanoandmore.com/AFM-Probe-ARROW-CONTR> (accessed on 10 April 2020).
110. Mathurin, J.; Dartois, E.; Engrand, C.; Duprat, J.; Deniset Besseau, A.; Dazzi, A.; Kebukawa, Y.; Noguchi, T.; Troadec, D. Nanometre-scale infrared chemical imaging (AFM-IR) of organic matter in ultra-carbonaceous antarctic micrometeorites (UCAMMS) and future analyses of hayabusa 2 samples. In Proceedings of the 51st Lunar and Planetary Science Conference, The Woodlands, TX, USA, 16–21 March 2020.
111. Lahiri, B.; Holland, G.; Centrone, A. Chemical imaging beyond the diffraction limit: Experimental validation of the PTIR technique. *Small* **2013**, *9*, 439–445. [[CrossRef](#)]
112. Dazzi, A.; Prazeres, R.; Glotin, F.; Ortega, J. Local infrared microspectroscopy with subwavelength spatial resolution with an atomic force microscope tip used as a photothermal sensor. *Opt. Lett.* **2005**, *30*, 2388–2390. [[CrossRef](#)]
113. Baden, N.; Yasuda, M.; Yoshida, A.; Muraki, N. New method for chemical characterization of polymer materials in industrial devices: AFM-IR with FIB sample preparation. In Proceedings of the IEEE 22nd International Symposium on the Physical and Failure Analysis of Integrated Circuits, Hsinchu, Taiwan, 29 June–2 July 2015; IEEE: Piscataway, NJ, USA, 2015; pp. 496–499.
114. Lu, F.; Belkin, M.A. Infrared absorption nano-spectroscopy using sample photoexpansion induced by tunable quantum cascade lasers. *Opt. Express* **2011**, *19*, 19942–19947. [[CrossRef](#)]
115. Frogley, M.D.; Lekkas, I.; Kelley, C.S.; Cinque, G. Performances for broadband synchrotron photothermal infrared nano-spectroscopy at Diamond Light Source. *Infrared Phys. Technol.* **2020**, *105*, 103238. [[CrossRef](#)]
116. Fukuoka, N.; Tanabe, K. Lightning-Rod Effect of Plasmonic Field Enhancement on Hydrogen-Absorbing Transition Metals. *Nanomaterials* **2019**, *9*, 1235. [[CrossRef](#)]
117. Rahaman, M.; Milekhin, A.G.; Mukherjee, A.; Rodyakina, E.E.; Latyshev, A.V.; Dzhagan, V.M.; Zahn, D.R. The role of a plasmonic substrate on the enhancement and spatial resolution of tip-enhanced Raman scattering. *Faraday Discuss.* **2019**, *214*, 309–323. [[CrossRef](#)] [[PubMed](#)]
118. Mathurin, J.; Pancani, E.; Deniset-Besseau, A.; Kjoller, K.; Prater, C.B.; Gref, R.; Dazzi, A. How to unravel the chemical structure and component localization of individual drug-loaded polymeric nanoparticles by using tapping AFM-IR. *Analyst* **2018**, *143*, 5940–5949. [[CrossRef](#)] [[PubMed](#)]
119. Wieland, K.; Ramer, G.; Weiss, V.U.; Allmaier, G.; Lendl, B.; Centrone, A. Nanoscale chemical imaging of individual chemotherapeutic cytarabine-loaded liposomal nanocarriers. *Nano Res.* **2019**, *12*, 197–203. [[CrossRef](#)] [[PubMed](#)]
120. Tuteja, M.; Kang, M.; Leal, C.; Centrone, A. Nanoscale partitioning of paclitaxel in hybrid lipid–polymer membranes. *Analyst* **2018**, *143*, 3808–3813. [[CrossRef](#)]
121. Dontsova, K.; Balogh-Brunstad, Z.; Roux, G.L. *Biogeochemical Cycles: Ecological Drivers and Environmental Impact*; Wiley: Hoboken, NJ, USA, 2020.
122. Harding, L.; King, W.P.; Dai, X.; Craig, D.Q.; Reading, M. Nanoscale characterisation and imaging of partially amorphous materials using local thermomechanical analysis and heated tip AFM. *Pharm. Res.* **2007**, *24*, 2048–2054. [[CrossRef](#)]
123. Bruker, A.I.C. nanoIR Nanoscale Thermal Analysis (nanoTA), nano-TA Uses a Heated AFM Tip to Measure Glass Transition and Melt Temperatures. Available online: <https://www.anasysinstruments.com/products/nanoir2/> (accessed on 14 April 2020).

124. Mamun, A.; Bazuin, C.G.; Prud'homme, R.E. Morphologies of Various Polycaprolactone/Polymer Blends in Ultrathin Films. *Macromolecules* **2015**, *48*, 1412–1417. [[CrossRef](#)]
125. Roland, S.; Gaspard, D.; Prud'homme, R.E.; Bazuin, C.G. Morphology Evolution in Slowly Dip-Coated Supramolecular PS-b-P4VP Thin Films. *Macromolecules* **2012**, *45*, 5463–5476. [[CrossRef](#)]
126. Chan, C.-M.; Li, L. Direct Observation of the Growth of Lamellae and Spherulites by AFM. In *Intrinsic Molecular Mobility and Toughness of Polymers II*; Springer: Berlin, Germany, 2005; pp. 1–41.
127. Schönherr, H.; Waymouth, R.M.; Frank, C.W. Nucleation and Crystallization of Low-Crystallinity Polypropylene Followed in Situ by Hot Stage Atomic Force Microscopy. *Macromolecules* **2003**, *36*, 2412–2418. [[CrossRef](#)]
128. Lei, Y.-G.; Chan, C.-M.; Li, J.-X.; Ng, K.-M.; Wang, Y.; Jiang, Y.; Li, L. The Birth of an Embryo and Development of the Founding Lamella of Spherulites As Observed by Atomic Force Microscopy. *Macromolecules* **2002**, *35*, 6751–6753. [[CrossRef](#)]
129. Schönherr, H.; Frank, C.W. Ultrathin Films of Poly(ethylene oxides) on Oxidized Silicon. 2. In Situ Study of Crystallization and Melting by Hot Stage AFM. *Macromolecules* **2003**, *36*, 1199–1208. [[CrossRef](#)]
130. Lei, Y.-G.; Chan, C.-M.; Wang, Y.; Ng, K.-M.; Jiang, Y.; Lin, L. Growth process of homogeneously and heterogeneously nucleated spherulites as observed by atomic force microscopy. *Polymer* **2003**, *44*, 4673–4679. [[CrossRef](#)]
131. Shtukenberg, A.G.; Punin, Y.O.; Gunn, E.; Kahr, B. Spherulites. *Chem. Rev.* **2012**, *112*, 1805–1838. [[CrossRef](#)] [[PubMed](#)]
132. Liu, Y.-X.; Chen, E.-Q. Polymer crystallization of ultrathin films on solid substrates. *Coord. Chem. Rev.* **2010**, *254*, 1011–1037. [[CrossRef](#)]
133. Taguchi, K.; Miyaji, H.; Izumi, K.; Hoshino, A.; Miyamoto, Y.; Kokawa, R. Crystal growth of isotactic polystyrene in ultrathin films: Film thickness dependence. *J. Macromol. Sci. Part B* **2002**, *41*, 1033–1042. [[CrossRef](#)]
134. Mullins, W.W.; Sekerka, R.F. Morphological Stability of a Particle Growing by Diffusion or Heat Flow. *J. Appl. Phys.* **1963**, *34*, 323–329. [[CrossRef](#)]
135. Prud'homme, R.E. Crystallization and morphology of ultrathin films of homopolymers and polymer blends. *Prog. Polym. Sci.* **2016**, *54–55*, 214–231.
136. Dazzi, A.; Prater, C.B.; Hu, Q.; Chase, D.B.; Rabolt, J.F.; Marcott, C. AFM–IR: Combining atomic force microscopy and infrared spectroscopy for nanoscale chemical characterization. *Appl. Spectrosc.* **2012**, *66*, 1365–1384. [[CrossRef](#)]
137. Prater, C.; Kjoller, K.; Cook, D.; Shetty, R.; Meyers, G.; Reinhardt, C.; Felts, J.; King, W.; Vodopyanov, K.; Dazzi, A. Nanoscale infrared spectroscopy of materials by atomic force microscopy. *Microsc. Anal. -UK* **2010**, *24*, 5–8.
138. Dazzi, A.; Glotin, F.; Carminati, R. Theory of infrared nanospectroscopy by photothermal induced resonance. *J. Appl. Phys.* **2010**, *107*, 124519. [[CrossRef](#)]
139. Katzenmeyer, A.M.; Aksyuk, V.; Centrone, A. Nanoscale infrared spectroscopy: Improving the spectral range of the photothermal induced resonance technique. *Anal. Chem.* **2013**, *85*, 1972–1979. [[CrossRef](#)]
140. Felts, J.R.; Kjoller, K.; Lo, M.; Prater, C.B.; King, W.P. Nanometer-scale infrared spectroscopy of heterogeneous polymer nanostructures fabricated by tip-based nanofabrication. *ACS Nano* **2012**, *6*, 8015–8021. [[CrossRef](#)] [[PubMed](#)]
141. Mayet, C.; Deniset-Besseau, A.; Prazeres, R.; Ortega, J.-M.; Dazzi, A. Analysis of bacterial polyhydroxybutyrate production by multimodal nanoimaging. *Biotechnol. Adv.* **2013**, *31*, 369–374. [[CrossRef](#)] [[PubMed](#)]
142. Kjoller, K.; Prater, C.; Shetty, R. Polymer Characterization: Using Nanoscale Infrared Spectroscopy. *Am. Lab.* **2010**, *42*, 20–23.
143. Ye, J.; Midorikawa, H.; Awatani, T.; Marcott, C.; Lo, M.; Kjoller, K.; Shetty, R. Nanoscale infrared spectroscopy and AFM imaging of a polycarbonate/acrylonitrile-styrene/butadiene blend. *Microsc. Anal.* **2012**, *26*, 24–27.
144. Felts, J.R.; Somnath, S.; Ewoldt, R.H.; King, W.P. Nanometer-scale flow of molten polyethylene from a heated atomic force microscope tip. *Nanotechnology* **2012**, *23*, 215301. [[CrossRef](#)] [[PubMed](#)]
145. Kenkel, S.; Mittal, A.; Mittal, S.; Bhargava, R. Probe–Sample Interaction-Independent Atomic Force Microscopy–Infrared Spectroscopy: Toward Robust Nanoscale Compositional Mapping. *Anal. Chem.* **2018**, *90*, 8845–8855. [[CrossRef](#)] [[PubMed](#)]

146. Van Eerdenbrugh, B.; Lo, M.; Kjoller, K.; Marcott, C.; Taylor, L.S. Nanoscale mid-infrared imaging of phase separation in a drug–polymer blend. *J. Pharm. Sci.* **2012**, *101*, 2066–2073. [[CrossRef](#)]
147. Barsbay, M.; Güner, A. Miscibility of dextran and poly (ethylene glycol) in solid state: Effect of the solvent choice. *Carbohydr. Polym.* **2007**, *69*, 214–223. [[CrossRef](#)]
148. Borodko, Y.; Habas, S.E.; Koebel, M.; Yang, P.; Frei, H.; Somorjai, G.A. Probing the Interaction of Poly (vinylpyrrolidone) with Platinum Nanocrystals by UV–Raman and FTIR. *J. Phys. Chem. B* **2006**, *110*, 23052–23059. [[CrossRef](#)]
149. Marcott, C.; Awatani, T.; Ye, J.; Gerrard, D.; Lod, M.; Kjoller, K. Review of nanoscale infrared spectroscopy applications to energy related materials. *Spectrosc. Eur.* **2014**, 19–23.
150. Tipduangta, P.; Belton, P.; Fabian, L.; Wang, L.Y.; Tang, H.; Eddleston, M.; Qi, S. Electrospun polymer blend nanofibers for tunable drug delivery: The role of transformative phase separation on controlling the release rate. *Mol. Pharm.* **2016**, *13*, 25–39. [[CrossRef](#)] [[PubMed](#)]
151. Li, N.; Taylor, L.S. Nanoscale infrared, thermal, and mechanical characterization of telaprevir–polymer miscibility in amorphous solid dispersions prepared by solvent evaporation. *Mol. Pharm.* **2016**, *13*, 1123–1136. [[CrossRef](#)] [[PubMed](#)]
152. Tang, F.; Bao, P.; Roy, A.; Wang, Y.; Su, Z. In-situ spectroscopic and thermal analyses of phase domains in high-impact polypropylene. *Polymer* **2018**, *142*, 155–163. [[CrossRef](#)]
153. Bro, R.; Smilde, A.K. Principal component analysis. *Anal. Methods* **2014**, *6*, 2812–2831. [[CrossRef](#)]
154. Jolliffe, I.T.; Cadima, J. Principal component analysis: A review and recent developments. *Philos. Trans. R. Soc. A Math. Phys. Eng. Sci.* **2016**, *374*, 20150202. [[CrossRef](#)] [[PubMed](#)]
155. Tognana, S.A.; Salgueiro, W.A.; Silva, L. A SAXS study of PHB/DGEBA blends crystallized at different temperatures. *Procedia Mater. Sci.* **2015**, *8*, 271–277. [[CrossRef](#)]
156. Reddy, K.R.; Ogawa, S.; Sato, H.; Takahashi, I.; Ozaki, Y. Evolution of intermediate and highly ordered crystalline states under spatial confinement in poly (3-hydroxybutyrate) ultrathin films. *Macromolecules* **2016**, *49*, 4202–4210.
157. Rosenthal, M.; Burghammer, M.; Bar, G.; Samulski, E.T.; Ivanov, D.A. Switching chirality of hybrid left–right crystalline helicoids built of achiral polymer chains: When right to left becomes left to right. *Macromolecules* **2014**, *47*, 8295–8304. [[CrossRef](#)]
158. Ivanov, D.A.; Rosenthal, M. Microstructure of banded polymer spherulites: New insights from synchrotron nanofocus X-ray scattering. In *Polymer Crystallization II*; Springer: Berlin, Germany, 2016; pp. 95–126.
159. Nguyen-Tri, P.; Prud'homme, R.E. Nanoscale lamellar assembly and segregation mechanism of poly (3-hydroxybutyrate)/poly (ethylene glycol) blends. *Macromolecules* **2018**, *51*, 181–188.
160. Nguyen Tri, P.; Prud'homme, R.E. Crystallization and Segregation Behavior at the Submicrometer Scale of PCL/PEG Blends. *Macromolecules* **2018**, *51*, 7266–7273. [[CrossRef](#)]
161. Nguyen-Tri, P.; Prud'homme, R.E. Nanoscale analysis of the photodegradation of Polyester fibers by AFM-IR. *J. Photochem. Photobiol. A Chem.* **2019**, *371*, 196–204. [[CrossRef](#)]
162. Zeb, G.; Nguyen-Tri, P.; Palacin, S.; Le, X.T. Pulse potential deposition of thick polyvinylpyridine-like film on the surface of titanium nitride. *RSC Adv.* **2016**, *6*, 80825–80829. [[CrossRef](#)]
163. Nguyen, T.V.; Le, X.H.; Dao, P.H.; Decker, C.; Nguyen-Tri, P. Stability of acrylic polyurethane coatings under accelerated aging tests and natural outdoor exposure: The critical role of the used photo-stabilizers. *Prog. Org. Coat.* **2018**, *124*, 137–146. [[CrossRef](#)]
164. Nguyen, T.V.; Tri, P.N.; Nguyen, T.D.; El Aidani, R.; Decker, C. Accelerated degradation of water borne acrylic nanocomposites used in outdoor protective coatings. *Polym. Degrad. Stab.* **2016**, *128*, 65–76. [[CrossRef](#)]
165. Nguyen-Tri, P.; El Aidani, R.; Leborgne, É.; Pham, T.; Vu-Khanh, T. Chemical ageing of a polyester nonwoven membrane used in aerosol and drainage filter. *Polym. Degrad. Stab.* **2014**, *101*, 71–80. [[CrossRef](#)]
166. El Aidani, R.; Nguyen-Tri, P.; Malajati, Y.; Lara, J.; Vu-Khanh, T. Photochemical aging of an e-PTFE/NOMEX® membrane used in firefighter protective clothing. *Polym. Degrad. Stab.* **2013**, *98*, 1300–1310. [[CrossRef](#)]
167. Yan, C.; Huang, W.; Ma, J.; Xu, J.; Lv, Q.; Lin, P. Characterizing the SBS polymer degradation within high content polymer modified asphalt using ATR-FTIR. *Constr. Build. Mater.* **2020**, *233*, 117708. [[CrossRef](#)]
168. Tsuji, H.; Sato, S.; Masaki, N.; Arakawa, Y.; Yoshizaki, Y.; Kuzuya, A.; Ohya, Y. Thermal properties and degradation of enantiomeric copolyesteramides poly(lactic acid-co-alanine)s. *Polym. Degrad. Stab.* **2020**, *171*, 109047. [[CrossRef](#)]

169. Wu, F.; Misra, M.; Mohanty, A.K. Tailoring the toughness of sustainable polymer blends from biodegradable plastics via morphology transition observed by atomic force microscopy. *Polym. Degrad. Stab.* **2020**, *173*, 109066. [[CrossRef](#)]
170. Xu, Y.; Li, P.; Li, L.; Dai, J.; Ran, Q.; Gu, Y. Thermal degradation mechanism of a cured acetylene/aldehyde functional benzoxazine with high thermal stability. *Polym. Degrad. Stab.* **2020**, *171*, 109041. [[CrossRef](#)]
171. Numata, K.; Asano, A.; Nakazawa, Y. Solid-state and time domain NMR to elucidate degradation behavior of thermally aged poly (urea-urethane). *Polym. Degrad. Stab.* **2020**, *172*, 109052. [[CrossRef](#)]
172. Wei, T.; Tang, Z.; Yu, Q.; Chen, H. Smart antibacterial surfaces with switchable bacteria-killing and bacteria-releasing capabilities. *ACS Appl. Mater. Interfaces* **2017**, *9*, 37511–37523. [[CrossRef](#)] [[PubMed](#)]
173. Brown, L.V.; Davanco, M.; Sun, Z.; Kretinin, A.; Chen, Y.; Matson, J.R.; Vurgaftman, I.; Sharac, N.; Giles, A.J.; Fogler, M.M. Nanoscale mapping and spectroscopy of nonradiative hyperbolic modes in hexagonal boron nitride nanostructures. *Nano Lett.* **2018**, *18*, 1628–1636. [[CrossRef](#)]
174. Morsch, S.; Lyon, S.; Greensmith, P.; Smith, S.; Gibbon, S. Mapping water uptake in organic coatings using AFM-IR. *Faraday Discuss.* **2015**, *180*, 527–542. [[CrossRef](#)] [[PubMed](#)]
175. Morsch, S.; Lyon, S.; Gibbon, S. The degradation mechanism of an epoxy-phenolic can coating. *Prog. Org. Coat.* **2017**, *102*, 37–43. [[CrossRef](#)]
176. Morsch, S.; Liu, Y.; Greensmith, P.; Lyon, S.B.; Gibbon, S.R. Molecularly controlled epoxy network nanostructures. *Polymer* **2017**, *108*, 146–153. [[CrossRef](#)]
177. Morsch, S.; Van Driel, B.A.; van den Berg, K.J.; Dik, J. Investigating the photocatalytic degradation of oil paint using ATR-IR and AFM-IR. *ACS Appl. Mater. Interfaces* **2017**, *9*, 10169–10179. [[CrossRef](#)]
178. Morsch, S.; Bastidas, P.D.; Rowland, S.M. AFM-IR insights into the chemistry of interfacial tracking. *J. Mater. Chem. A* **2017**, *5*, 24508–24517. [[CrossRef](#)]
179. Shiraishi, F.; Maruoka, D.; Tanoue, Y. A better UV light and TiO₂-PET sheet arrangement for enhancing photocatalytic decomposition of volatile organic compounds. *Separat. Purif. Technol.* **2017**, *175*, 185–193. [[CrossRef](#)]
180. Hurley, C.R.; Leggett, G.J. Quantitative investigation of the photodegradation of polyethylene terephthalate film by friction force microscopy, contact-angle goniometry, and X-ray photoelectron spectroscopy. *ACS Appl. Mater. Interfaces* **2009**, *1*, 1688–1697. [[CrossRef](#)]



© 2020 by the authors. Licensee MDPI, Basel, Switzerland. This article is an open access article distributed under the terms and conditions of the Creative Commons Attribution (CC BY) license (<http://creativecommons.org/licenses/by/4.0/>).